Computational Mechanics (2021) 68:1–24
https://doi.org/10.1007/s00466-021-02002-8

ORIGINAL PAPER

A hybrid $H^1 \times H(\mathrm{curl})$ finite element formulation for a relaxed micromorphic continuum model of antiplane shear

Adam Sky[1] · Michael Neunteufel[2] · Ingo Münch[3] · Joachim Schöberl[2] · Patrizio Neff[4]

Received: 29 September 2020 / Accepted: 27 February 2021 / Published online: 17 May 2021

Abstract

One approach for the simulation of metamaterials is to extend an associated continuum theory concerning its kinematic equations, and the relaxed micromorphic continuum represents such a model. It incorporates the Curl of the nonsymmetric microdistortion in the free energy function. This suggests the existence of solutions not belonging to H^1, such that standard nodal H^1-finite elements yield unsatisfactory convergence rates and might be incapable of finding the exact solution. Our approach is to use base functions stemming from both Hilbert spaces H^1 and $H(\mathrm{curl})$, demonstrating the central role of such combinations for this class of problems. For simplicity, a reduced two-dimensional relaxed micromorphic continuum describing antiplane shear is introduced, preserving the main computational traits of the three-dimensional version. This model is then used for the formulation and a multi step investigation of a viable finite element solution, encompassing examinations of existence and uniqueness of both standard and mixed formulations and their respective convergence rates.

Keywords Relaxed micromorphic continuum · Edge elements · Nédélec elements · Curl based energy · Mixed formulation · Combined Hilbert spaces · Metamaterials

1 Introduction

Materials with a pronounced microstructure such as metamaterials, see e.g. [2,3,7,19], porous media, composites etc., activate micro-motions which are not accounted for in classical continuum mechanics, where each material point is equipped with only three translational degrees of freedom. Therefore, several approaches to model such materials can be found in literature, such as multi-scale finite element methods [1,10,11] or generalized continuum theories. The latter can be classified into higher gradient theories [5,17,23,32] and so called micromorphic continuum theories [30,42]. These theories extend the kinematics of the material point. Depending on the extension one obtains for example micropolar [16,25,26], microstretch [38] or microstrain [13,15] theories. In its most general setting, as introduced by Eringen und Mindlin [12,22], a micromorphic continuum theory allows the material point to undergo an affine distortion independent of its macroscopic deformation arising from the displacement field. Consequently, in the micromorphic theory a material point is considered with $3 + 9 = 12$ degrees of freedom, of which the microdistortion $\boldsymbol{P}$ encompasses 9. The various micromorphic theories differ in their proposition of the free energy functional. While classical theories incorporate

✉ Adam Sky
adam.sky@tu-dortmund.de

Michael Neunteufel
michael.neunteufel@tuwien.ac.at

Ingo Münch
ingo.muench@tu-dortmund.de

Joachim Schöberl
joachim.schoeberl@tuwien.ac.at

Patrizio Neff
patrizio.neff@uni-due.de

1 Chair of Statics and Dynamics, Technische Universität Dortmund, August-Schmidt-Str. 8, 44227 Dortmund, Germany

2 Institute for Analysis and Scientific Computing, Technische Universität Wien, Wiedner Hauptstr. 8-10, 1040 Wien, Austria

3 Head of Chair of Statics and Dynamics, Technische Universität Dortmund, August-Schmidt-Str. 8, 44227 Dortmund, Germany

4 Head of Chair for Nonlinear Analysis and Modelling, Faculty of Mathematics, Universität Duisburg-Essen, Thea-Leymann Str. 9, 45127 Essen, Germany

the full gradient of the microdistortion $\nabla \boldsymbol{P}$ into the energy function [31], the relaxed micromorphic theory [20,31,33,34] considers only Curl $\boldsymbol{P}$. The incorporation of the Curl of the microdistortion, formally known as the dislocation density, into the free energy functional relaxes the continuity assumptions on the microdistortion and enlarges the space of possible weak solutions, i.e. $[H^1]^3 \times H(\text{Curl})$. Furthermore, the relaxed micromorphic theory aspires to capture the entire spectrum of mechanical behaviour between the macro and micro scale of the material. This is achieved via homogenization of the material parameters and the introduction of the characteristic length L_c [19,29], which determines the influence of the dislocation density in the free energy functional. Specific analytical solutions to the full isotropic relaxed micromorphic model are presented in [35–37].

For non-trivial boundary value problems, solutions of continuum theories are approximated via the finite element method. While the standard Lagrange elements are well suited for solutions in H^1, solutions in $H(\text{curl})$ may require a different class of elements, depending on the problem at hand. The lowest class of finite elements in $H(\text{curl})$, sometimes called edge elements, have been derived by Nédélec [27,28]. Extensions to higher order element formulations can be found in [8,9,41,44]. In this paper we consider finite element formulations employing either $H^1 \times [H^1]^2$ or $H^1 \times H(\text{curl})$ and investigate their validity in correctly approximating results in the relaxed micromorphic continuum. Furthermore, we test both a primal and mixed formulation of the corresponding boundary problem for increasingly large values of the characteristic length L_c. To that end, we consider a planar version of the relaxed micromorphic continuum, namely of antiplane shear [43]. More precisely, the matrix-Curl in 3D reduces to a scalar-curl of the microdistortion in 2D. However, the results of our investigation directly apply to the full three-dimensional version.

The paper is organized as follows: In the following section we introduce the planar relaxed micromorphic continuum. Section 3 is devoted to prove solvability of the primal and mixed problem and discussing properties in the limit case $L_c \to \infty$, in both the continuous and discrete settings, respectively. In Section 4 we present appropriate base functions for $H(\text{curl})$, the corresponding covariant Piola transformation for Nédélec finite elements and the resulting stiffness matrices. Finally, we present several numerical examples to confirm the theoretical results.

2 The planar relaxed micromorphic continuum

The free energy functional of the relaxed micromorphic continuum [29,31] incorporates the gradient of the displacement field, the microdistortion and its Curl

$$
\begin{aligned}
I(\mathbf{u}, \boldsymbol{P}) = \frac{1}{2} \int_\Omega & \langle \mathbb{C}_e \operatorname{sym}(\nabla \mathbf{u} - \boldsymbol{P}),\ \operatorname{sym}(\nabla \mathbf{u} - \boldsymbol{P}) \rangle \\
& + \langle \mathbb{C}_{\text{micro}} \operatorname{sym} \boldsymbol{P},\ \operatorname{sym} \boldsymbol{P} \rangle \\
& + \langle \mathbb{C}_c \operatorname{skew}(\nabla \mathbf{u} - \boldsymbol{P}),\ \operatorname{skew}(\nabla \mathbf{u} - \boldsymbol{P}) \rangle \\
& + \frac{\mu_{\text{macro}} L_c^2}{2} \|\operatorname{Curl} \boldsymbol{P}\|^2 - \langle \mathbf{f},\ \mathbf{u} \rangle - \langle \boldsymbol{M},\ \boldsymbol{P} \rangle \, \mathrm{d}X \,,
\end{aligned}
\tag{2.1}
$$

$$
\nabla \mathbf{u} = \begin{bmatrix} u_{1,1} & u_{1,2} & u_{1,3} \\ u_{2,1} & u_{2,2} & u_{2,3} \\ u_{3,1} & u_{3,2} & u_{3,3} \end{bmatrix}, \quad \operatorname{Curl} \boldsymbol{P} = \begin{bmatrix} (\operatorname{curl} \begin{bmatrix} P_{11} & P_{12} & P_{13} \end{bmatrix})^T \\ (\operatorname{curl} \begin{bmatrix} P_{21} & P_{22} & P_{23} \end{bmatrix})^T \\ (\operatorname{curl} \begin{bmatrix} P_{31} & P_{32} & P_{33} \end{bmatrix})^T \end{bmatrix},
$$

$$
\operatorname{curl} \mathbf{v} = \nabla \times \mathbf{v} \,, \tag{2.2}
$$

with $\mathbf{u} : \Omega \subset \mathbb{R}^3 \to \mathbb{R}^3$ and $\boldsymbol{P} : \Omega \subset \mathbb{R}^3 \to \mathbb{R}^{3\times 3}$ representing the displacement and the non-symmetric microdistortion, respectively. Here, $\mathbb{C}_e$ and $\mathbb{C}_{\text{micro}}$ are standard elasticity tensors and $\mathbb{C}_c$ is a positive semi-definite coupling tensor for rotations. The macroscopic shear modulus is denoted by μ_{macro} and the parameter $L_c \geq 0$ represents the characteristic length scale motivated by the microstructure.

From now on, we consider the planar reduction of this continuum to antiplane shear, still capturing the main mathematical aspects of the three-dimensional version, namely the additional microdistortion and the curl

$$
\begin{aligned}
I(u, \boldsymbol{\zeta}) = & \int_\Omega \mu_e \|\nabla u - \boldsymbol{\zeta}\|^2 + \mu_{\text{micro}} \|\boldsymbol{\zeta}\|^2 \\
& + \mu_{\text{macro}} \frac{L_c^2}{2} \|\operatorname{curl}_{2D} \boldsymbol{\zeta}\|^2 - \langle u,\ f \rangle \\
& - \langle \boldsymbol{\zeta},\ \boldsymbol{\omega} \rangle \, \mathrm{d}X \,, \quad \Omega \subset \mathbb{R}^2 \,,
\end{aligned}
\tag{2.3}
$$

where we employ the two-dimensional definitions of the curl and gradient operators

$$
\begin{aligned}
& \operatorname{curl}_{2D} \boldsymbol{\zeta} = \zeta_{2,1} - \zeta_{1,2} \,, \quad \boldsymbol{\zeta} \in \mathbb{R}^2 \,, \\
& \mathrm{D}^{\text{curl}}(u) = \begin{bmatrix} u_{,2} \\ -u_{,1} \end{bmatrix}, \, u \in \mathbb{R} \,, \\
& \nabla u = \begin{bmatrix} u_{,1} \\ u_{,2} \end{bmatrix}, \quad u \in \mathbb{R} \,.
\end{aligned}
\tag{2.4}
$$

In Eq. (2.3) we reduced the displacement to a scalar field $u : \Omega \subset \mathbb{R}^2 \to \mathbb{R}$ and the microdistortion $\boldsymbol{P}$ to a vector field $\boldsymbol{\zeta} : \Omega \subset \mathbb{R}^2 \to \mathbb{R}^2$. The displacement field u is now perpendicular to the plane of the domain. The elasticity tensors $\mathbb{C}_e$ and $\mathbb{C}_{\text{micro}}$ are replaced by the scalars μ_e, $\mu_{\text{micro}} > 0$ and $\mathbb{C}_c$ no longer appears.

Remark 2.1 The simplification of the model to antiplane shear serves to facilitate the mathematical analysis of the model and allows for a thorough investigation of the numerical behaviour of finite element solutions in the relaxed

micromorphic theory. Whether this **reduced** model can be applied to real-world metamaterials is unclear at this time. For applications of the **full** three-dimensional theory see [19,20].

In order to find functions minimizing the potential energy I we calculate the variations with respect to u and $\boldsymbol{\zeta}$

$$\int_\Omega 2\mu_\mathrm{e}\langle(\nabla u - \boldsymbol{\zeta}),\ \nabla\delta u\rangle\,\mathrm{d}X = \int_\Omega \langle \delta u,\ f\rangle\,\mathrm{d}X\,, \tag{2.5a}$$

$$\begin{aligned}&\int_\Omega 2\mu_\mathrm{e}\,\langle(\nabla u - \boldsymbol{\zeta}),\ (-\delta\boldsymbol{\zeta})\rangle + 2\mu_\mathrm{micro}\,\langle\boldsymbol{\zeta},\ \delta\boldsymbol{\zeta}\rangle\\ &\quad + \mu_\mathrm{macro}\,L_\mathrm{c}^2\,\langle\mathrm{curl}_\mathrm{2D}\,\boldsymbol{\zeta},\ \mathrm{curl}_\mathrm{2D}\,\delta\boldsymbol{\zeta}\rangle\,\mathrm{d}X = \int_\Omega \langle\delta\boldsymbol{\zeta},\ \boldsymbol{\omega}\rangle\,\mathrm{d}X\,.\end{aligned} \tag{2.5b}$$

Partial integration of Eq. (2.5a) and Eq. (2.5b) yields the strong form including boundary conditions (see Appendix A for more details)

$$-2\mu_\mathrm{e}\,\mathrm{div}(\nabla u - \boldsymbol{\zeta}) = f \quad \text{in } \Omega\,, \tag{2.6a}$$

$$\begin{aligned}&-2\mu_\mathrm{e}(\nabla u - \boldsymbol{\zeta}) + 2\mu_\mathrm{micro}\boldsymbol{\zeta}\\ &\quad + \mu_\mathrm{macro}L_\mathrm{c}^2\,\mathrm{D}^\mathrm{curl}(\mathrm{curl}_\mathrm{2D}\,\boldsymbol{\zeta}) = \boldsymbol{\omega} \quad \text{in } \Omega\,,\end{aligned} \tag{2.6b}$$

$$u = \widetilde{u} \quad \text{on } \Gamma_D^u\,, \tag{2.6c}$$

$$\langle\boldsymbol{\zeta},\ \boldsymbol{\tau}\rangle = \langle\widetilde{\boldsymbol{\zeta}},\ \boldsymbol{\tau}\rangle \quad \text{on } \Gamma_D^\zeta\,, \tag{2.6d}$$

$$\langle\nabla u,\ \boldsymbol{\nu}\rangle = \langle\boldsymbol{\zeta},\ \boldsymbol{\nu}\rangle \quad \text{on } \Gamma_N^u\,, \tag{2.6e}$$

$$\mathrm{curl}_\mathrm{2D}\,\boldsymbol{\zeta} = 0 \quad \text{on } \Gamma_N^\zeta\,, \tag{2.6f}$$

where $\boldsymbol{\tau}$ and $\boldsymbol{\nu}$ denote the outer tangent and normal vector on the boundary, see Fig. 1, and with $\widetilde{u}$ and $\widetilde{\boldsymbol{\zeta}}$ the displacement and microdistortion fields on Γ_D^u and Γ_D^ζ are prescribed. From a mathematical point of view, it is possible to prescribe the tangential components of the microdistortion $\boldsymbol{\zeta}$ on the boundary Γ_D^ζ. This is used to test our numerical formulation in Sect. 5. However, from the point of view of physics it is impossible to control the microdistortion of the continuum with no direct relation to the displacement u and as such, the **consistent coupling condition** $\langle\boldsymbol{\zeta},\ \boldsymbol{\tau}\rangle = \langle\nabla\widetilde{u},\ \boldsymbol{\tau}\rangle$ arises on the Dirichlet boundary, being common to both u and $\boldsymbol{\zeta}$, enforcing the condition $\Gamma_D^\zeta \subset \Gamma_D^u$. Furthermore, Dirichlet boundary data for the microdistortion $\boldsymbol{\zeta}$ are not required for the existence of a unique solution here, as coercivity in the appropriate spaces is still determined.

3 Solvability and limit problems

3.1 Continuous case

In this section we prove the existence and uniqueness of the weak form of the planar relaxed micromorphic continuum.

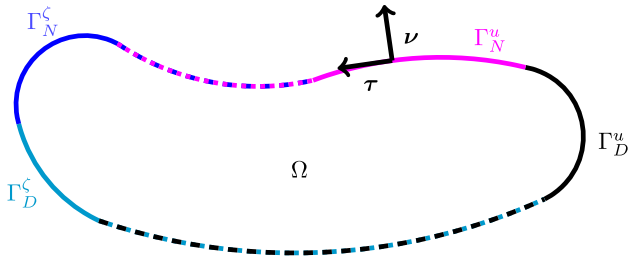

Fig. 1 Outer tangent $\boldsymbol{\tau}$ and normal vector $\boldsymbol{\nu}$ on the boundary of the domain Ω

Further, the corresponding mixed formulation is presented, whose coercivity constant is independent of L_c. Finally, we study necessary and sufficient conditions such that $\nabla u = \boldsymbol{\zeta}$ is guaranteed in the limit $L_\mathrm{c} \to \infty$. For simplicity, we assume homogeneous Dirichlet conditions on the entire boundary throughout this section, i.e., $u = 0$ and $\langle\boldsymbol{\zeta},\ \boldsymbol{\tau}\rangle = 0$ on $\Gamma_D^u = \Gamma_D^\zeta = \partial\Omega$, and mention that the proof can be readily adapted for inhomogeneous and mixed boundary conditions as long as the Dirichlet boundary for the displacements is non-trivial, $|\Gamma_D^u| > 0$, [14].

We define the following Hilbert spaces and their respective norms

$$\begin{aligned}H^1(\Omega) &= \{u \in L^2(\Omega)\,|\,\nabla u \in L^2(\Omega)^2\}\,,\\ \|u\|_{H^1}^2 &= \|u\|_{L^2}^2 + \|\nabla u\|_{L^2}^2\,,\end{aligned} \tag{3.1a}$$

$$H_0^1(\Omega) = \{u \in H^1(\Omega)\,|\,u = 0 \text{ on } \partial\Omega\}\,, \tag{3.1b}$$

$$\begin{aligned}H(\mathrm{curl},\,\Omega) &= \{\boldsymbol{\zeta} \in L^2(\Omega)^2\,|\,\mathrm{curl}_\mathrm{2D}\,\boldsymbol{\zeta} \in L^2(\Omega)\}\,,\\ \|\boldsymbol{\zeta}\|_{H(\mathrm{curl})}^2 &= \|\boldsymbol{\zeta}\|_{L^2}^2 + \|\,\mathrm{curl}_\mathrm{2D}\,\boldsymbol{\zeta}\|_{L^2}^2\,,\end{aligned} \tag{3.1c}$$

$$H_0(\mathrm{curl},\,\Omega) = \{\boldsymbol{\zeta} \in H(\mathrm{curl},\ \Omega)\,|\,\langle\boldsymbol{\zeta},\ \boldsymbol{\tau}\rangle = 0 \text{ on } \partial\Omega\}\,, \tag{3.1d}$$

which are based on the Lebesgue norm and space

$$\begin{aligned}\|u\|_{L^2}^2 &= \int_\Omega \|u\|^2\,\mathrm{d}X\\ L^2(\Omega) &= \{u : \Omega \to \mathbb{R}\,|\,\|u\|_{L^2} < \infty\}\,,\\ L_0^2(\Omega) &= \left\{u \in L^2(\Omega)\,|\,\int_\Omega u\,\mathrm{d}X = 0\right\}\,.\end{aligned} \tag{3.2}$$

Further, we use the product space $X = H_0^1(\Omega) \times H_0(\mathrm{curl},\,\Omega)$ with the norm

$$\|\{u,\boldsymbol{\zeta}\}\|_X = \|u\|_{H^1} + \|\boldsymbol{\zeta}\|_{H(\mathrm{curl})}\,, \tag{3.3}$$

to define the following minimization problem[1]: Find $\{u,\boldsymbol{\zeta}\} \in X$ such that for all $\{\delta u,\delta\boldsymbol{\zeta}\} \in X$

[1] Note carefully that u and $\boldsymbol{\zeta}$ are two independent variables and lead to a minimization problem despite the resemblance to mixed formulations, i.e. saddle-point problems.

$$\underbrace{\int_\Omega 2\mu_e\langle(\nabla u - \boldsymbol{\zeta}),\ (\nabla\delta u - \delta\boldsymbol{\zeta})\rangle + 2\mu_{\text{micro}}\,\langle\boldsymbol{\zeta},\ \delta\boldsymbol{\zeta}\rangle + \mu_{\text{macro}}\,L_c^2\,\langle\text{curl}_{2D}\,\boldsymbol{\zeta},\ \text{curl}_{2D}\,\delta\boldsymbol{\zeta}\rangle\,\mathrm{d}X}_{=a(\{u,\boldsymbol{\zeta}\},\{\delta u,\delta\boldsymbol{\zeta}\})} = \int_\Omega \langle\delta u,\ f\rangle + \langle\delta\boldsymbol{\zeta},\ \boldsymbol{\omega}\rangle\,\mathrm{d}X\,, \tag{3.4}$$

In order to show the existence of unique solutions we consider the Lax–Milgram theorem.

Theorem 3.1 *If $\mu_e, \mu_{\text{micro}}, \mu_{\text{macro}}, L_c > 0$, then Problem 3.4 has a unique solution $\{u,\boldsymbol{\zeta}\} \in X$ and there holds the stability estimate*

$$\|\{u,\boldsymbol{\zeta}\}\|_X \le \frac{1}{\beta}\Big(\|f\|_{L^2} + \|\boldsymbol{\omega}\|_{L^2}\Big)\,,$$

with $\beta = \beta(\mu_e, \mu_{\text{micro}}, \mu_{\text{macro}}, L_c) > 0$.

Proof Using Cauchy–Schwarz and triangle inequality yields the continuity of $a(\cdot,\cdot)$

$$\begin{aligned}
|a(\{u,\boldsymbol{\zeta}\},\{\delta u,\delta\boldsymbol{\zeta}\})| &\le 2\mu_e\|\nabla u - \boldsymbol{\zeta}\|_{L^2}\|\nabla\delta u - \delta\boldsymbol{\zeta}\|_{L^2}\\
&+ 2\mu_{\text{micro}}\|\boldsymbol{\zeta}\|_{L^2}\|\delta\boldsymbol{\zeta}\|_{L^2}\\
&+ \mu_{\text{macro}}L_c^2\|\,\text{curl}_{2D}\,\boldsymbol{\zeta}\|_{L^2}\,\|\,\text{curl}_{2D}\,\delta\boldsymbol{\zeta}\|_{L^2}\\
&\le c_1\Big(\Big(\|\nabla u\|_{L^2} + \|\boldsymbol{\zeta}\|_{L^2}\Big)\Big(\|\nabla\delta u\|_{L^2} + \|\delta\boldsymbol{\zeta}\|_{L^2}\Big)\\
&+ \|\boldsymbol{\zeta}\|_{L^2}\|\delta\boldsymbol{\zeta}\|_{L^2} + \|\,\text{curl}_{2D}\,\boldsymbol{\zeta}\|_{L^2}\|\,\text{curl}_{2D}\,\delta\boldsymbol{\zeta}\|_{L^2}\Big)\\
&\le 3\,c_1\|\{u,\boldsymbol{\zeta}\}\|_X\|\{\delta u,\delta\boldsymbol{\zeta}\}\|_X\,,
\end{aligned} \tag{3.5}$$

for all $\{u,\boldsymbol{\zeta}\},\{\delta u,\delta\boldsymbol{\zeta}\} \in X$ with the constant $c_1 = \max\{2\mu_e, 2\mu_{\text{micro}}, \mu_{\text{macro}}L_c^2\}$.

By employing Young's[2] and Poincaré-Friedrich's[3] inequalities we show the bilinear form to be coercive

$$\begin{aligned}
a(\{u,\boldsymbol{\zeta}\},\{u,\boldsymbol{\zeta}\}) &= 2\mu_e\Big(\|\nabla u\|_{L^2}^2 + \|\boldsymbol{\zeta}\|_{L^2}^2 - 2\langle\nabla u,\boldsymbol{\zeta}\rangle_{L^2}\Big)\\
&+ 2\mu_{\text{micro}}\|\boldsymbol{\zeta}\|_{L^2}^2 + \mu_{\text{macro}}\,L_c^2\|\,\text{curl}_{2D}\,\boldsymbol{\zeta}\|_{L^2}^2\\
&\ge 2\mu_e\Big(\|\nabla u\|_{L^2}^2 + \|\boldsymbol{\zeta}\|_{L^2}^2 - \varepsilon\|\nabla u\|_{L^2}^2 - \frac{1}{\varepsilon}\|\boldsymbol{\zeta}\|_{L^2}^2\Big)\\
&+ 2\mu_{\text{micro}}\|\boldsymbol{\zeta}\|_{L^2}^2 + \mu_{\text{macro}}\,L_c^2\|\,\text{curl}_{2D}\,\boldsymbol{\zeta}\|_{L^2}^2\\
&\ge c_3\Big(\|\nabla u\|_{L^2}^2 + \|\boldsymbol{\zeta}\|_{L^2}^2 + \|\,\text{curl}_{2D}\,\boldsymbol{\zeta}\|_{L^2}^2\Big)\\
&\ge \frac{c_3}{2}\min\left\{1, \frac{1}{1+c_F^2}\right\}\|\{u,\boldsymbol{\zeta}\}\|_X^2\,,
\end{aligned} \tag{3.6}$$

when the constant ε is chosen as $1 > \varepsilon > \dfrac{\mu_e}{\mu_e + \mu_{\text{micro}}}$, which is possible for $\mu_e, \mu_{\text{micro}} > 0$. Consequently, the coercivity constant reads

$$\begin{aligned}
\beta &= \frac{c_3}{2}\min\left\{1, \frac{1}{1+c_F^2}\right\},\\
c_3 &= \min\left\{2\mu_e(1-\varepsilon), 2\mu_e\left(1-\frac{1}{\varepsilon}\right) + 2\mu_{\text{micro}},\ \mu_{\text{macro}}L_c^2\right\}.
\end{aligned} \tag{3.7}$$

This finishes the proof. □

Remark 3.1 Note, that the proof fails when taking instead $X = H_0^1(\Omega) \times [H_0^1(\Omega)]^2$ as $a(\cdot,\cdot)$ is then no longer coercive in this space because one cannot find a constant $c > 0$ such that $\|\boldsymbol{\zeta}\|_{L^2}^2 + \|\,\text{curl}_{2D}\,\boldsymbol{\zeta}\|_{L^2}^2 \ge c\,\|\boldsymbol{\zeta}\|_{H^1}^2$, for all $\boldsymbol{\zeta} \in [H_0^1(\Omega)]^2$. As $[H^1(\Omega)]^2$ is dense in $H(\text{curl},\Omega)$, we might expect convergence for $\boldsymbol{\zeta} \in [H^1(\Omega)]^2$, however, at the cost of sub-optimal convergence rates in the discretized setting. We present numerical examples, where the exact solution is in $H(\text{curl},\Omega)$ but not in $[H^1(\Omega)]^2$ observing only slow convergence. If the exact solution is smooth, i.e. $\boldsymbol{\zeta}$ is also in $[H^1(\Omega)]^2$, optimal convergence is observed.

An important aspect of the relaxed micromorphic continuum is its relation to the classical continuum theory (linear elasticity). This relation is governed by the material constants, where the characteristic length L_c plays a significant role. We are therefore interested in robust computations with respect to L_c.

The following result characterizes the conditions when a trivial solution with respect to L_c is expected.

Theorem 3.2 *Assume that the requirements of Theorem 3.1 are fulfilled. Further, let $\boldsymbol{\omega} = \nabla r$ be a gradient field, then, the microdistortion $\boldsymbol{\zeta}$ is compatible, i.e. $\boldsymbol{\zeta} = \nabla\chi$ and the solution $\{u,\boldsymbol{\zeta}\} \in X$ is independent of the parameter L_c.*

Proof We make the ansatz $\boldsymbol{\zeta} = \nabla\chi$, $\chi \in H^1(\Omega)$ and insert it in Problem 3.4 choosing $\delta u = 0$

$$\begin{aligned}
&\int_\Omega 2\mu_e\langle\nabla\chi - \nabla u,\ \delta\boldsymbol{\zeta}\rangle + 2\mu_{\text{micro}}\langle\nabla\chi,\ \delta\boldsymbol{\zeta}\rangle\,\mathrm{d}X\\
&= \int_\Omega \langle\nabla r, \delta\boldsymbol{\zeta}\rangle\,\mathrm{d}X \quad \text{for all } \delta\boldsymbol{\zeta}.
\end{aligned}$$

[2] Young: $-v\,w \ge -\left(\dfrac{\varepsilon\,v^2}{2} + \dfrac{w^2}{2\varepsilon}\right)\,, \quad \forall\varepsilon > 0\,, v, w \in \mathbb{R}$

[3] Poincaré-Friedrich: $\exists c_F > 0 : \|v\|_{L^2} \le c_F\|\nabla v\|_{L^2}, \forall v \in H_0^1(\Omega)$

We can express

$$\nabla\chi = \frac{1}{2(\mu_e + \mu_{micro})}\,(\nabla r + 2\mu_e \nabla u) \tag{3.8}$$

and inserting into Problem 3.4 choosing $\delta\boldsymbol{\zeta} = 0$ gives the following Laplace problem for u

$$\int_\Omega \frac{2\mu_e\,\mu_{micro}}{\mu_e + \mu_{micro}} \langle \nabla u, \nabla \delta u\rangle \,\mathrm{d}X = \int_\Omega f\,\delta u + \frac{\mu_e}{\mu_e + \mu_{micro}} \langle \nabla r, \nabla \delta u\rangle \,\mathrm{d}X \quad \text{for all } \delta u\,,$$

which is uniquely solvable. Since by Lax–Milgram the solution is unique, $\boldsymbol{\zeta} = \nabla\chi$ and the resulting u are the only possible solutions. According to Eq. (3.8) the solution of Problem 3.4 is given independently of L_c. □

Considering the limit case $L_c = 0$, the continuity of the bilinear form $a(\cdot,\cdot)$ follows automatically from Eq. (3.5). However, for coercivity to hold, the space for $\boldsymbol{\zeta}$ must be changed to $[L^2(\Omega)]^2$, i.e., the regularity of $\boldsymbol{\zeta}$ is lost.

Theorem 3.3 *If $\mu_e, \mu_{micro} > 0$ and $L_c = 0$ Problem 3.4 has a unique solution $\{u, \boldsymbol{\zeta}\} \in H^1_0(\Omega) \times [L^2(\Omega)]^2$. Further, if the right-hand side $\boldsymbol{\omega} = \nabla r$ is a gradient field with $r \in H^1(\Omega)$, the microdistortion $\boldsymbol{\zeta}$ results in a gradient field $\boldsymbol{\zeta} = \nabla\chi$ with $\chi \in H^1(\Omega)$. Especially, there holds the regularity result $\boldsymbol{\zeta} \in H(\mathrm{curl}, \Omega)$.*

Proof The proof of existence and uniqueness follows exactly the same lines as the proof of Theorem 3.1. If $\boldsymbol{\omega} = \nabla r$ we can conclude as in the proof of Theorem 3.2 that $\boldsymbol{\zeta}$ is a gradient field. □

Remark 3.2 Using Theorem 3.2 and assuming $\boldsymbol{\omega} = 0$, we can reformulate Eq. (2.6b) to retrieve $\boldsymbol{\zeta}$ from the known field u

$$\boldsymbol{\zeta} = \nabla\chi = \frac{\mu_e}{\mu_{micro} + \mu_e}\nabla u\,. \tag{3.9}$$

Furthermore, we can condensate Eq. (2.6a) into the Poisson equation

$$-\operatorname{div}\left(\frac{2\mu_e\,\mu_{micro}}{\mu_e + \mu_{micro}}\nabla u\right) = \underbrace{\left(\frac{-2\mu_e\,\mu_{micro}}{\mu_e + \mu_{micro}}\right)}_{=-2\,\mu_{macro}} \Delta u = -2\,\mu_{macro}\,\Delta u = f\,, \tag{3.10}$$

where the homogenization of the material constants follows as in [29]. We notice, that Theorem 3.2 and Theorem 3.3 imply the field u is always independent of the microdistortion $\boldsymbol{\zeta}$ in this setting. In the condensed state, the relation of the model with antiplane shear for membranes is apparent.

Remark 3.3 We note that the previous result does not hold in the full three-dimensional relaxed micromorphic continuum, i.e. the absence of external moments does not automatically imply $\boldsymbol{P} = \nabla\boldsymbol{\chi}$ for $\boldsymbol{\chi} \in [H^1(\Omega)]^3$.

Having considered the limit of the characteristic length $L_c \to 0$, we reformulate Problem 3.4 as an equivalent mixed formulation in order to examine its limit for $L_c \to \infty$. We start by introducing the new variable

$$m = \mu_{macro}\,L_c^2\,\mathrm{curl}_{2D}\,\boldsymbol{\zeta} \in L^2_0(\Omega), \tag{3.11}$$

and constructing a new bilinear form by multiplying it with a test function

$$\int_\Omega \langle \mathrm{curl}_{2D}\,\boldsymbol{\zeta}, \delta m\rangle - \frac{1}{\mu_{macro}\,L_c^2}\langle m, \delta m\rangle \,\mathrm{d}X = 0 \quad \text{for all } \delta m \in L^2_0(\Omega)\,. \tag{3.12}$$

The restriction to $m \in L^2_0(\Omega)$ follows from the Stoke's theorem

$$\int_\Omega \mathrm{curl}_{2D}\,\boldsymbol{\zeta}\,\mathrm{d}X = \oint_{\partial\Omega} \langle \boldsymbol{\zeta},\ \boldsymbol{\tau}\rangle\,\mathrm{d}s = 0 \quad \text{for all } \boldsymbol{\zeta} \in H_0(\mathrm{curl}, \Omega)\,. \tag{3.13}$$

We introduce the (bi-)linear forms

$$a(\{u, \boldsymbol{\zeta}\}, \{\delta u, \delta\boldsymbol{\zeta}\}) = \int_\Omega 2\mu_e\langle(\nabla u - \boldsymbol{\zeta}), (\nabla\delta u - \delta\boldsymbol{\zeta})\rangle + 2\mu_{micro}\,\langle \boldsymbol{\zeta}, \delta\boldsymbol{\zeta}\rangle\,\mathrm{d}X\,, \tag{3.14a}$$

$$b(\{u, \boldsymbol{\zeta}\}, \delta m) = \int_\Omega \langle \mathrm{curl}_{2D}\,\boldsymbol{\zeta}, \delta m\rangle\,\mathrm{d}X\,, \tag{3.14b}$$

$$c(m, \delta m) = \int_\Omega \langle m, \delta m\rangle\,\mathrm{d}X\,, \tag{3.14c}$$

$$d(\{\delta u, \delta\boldsymbol{\zeta}\}) = \int_\Omega \langle \delta u,\ f\rangle + \langle \delta\boldsymbol{\zeta},\ \boldsymbol{\omega}\rangle\,\mathrm{d}X\,, \tag{3.14d}$$

and the resulting mixed formulation reads: find $(\{u, \boldsymbol{\zeta}\}, m) \in X \times L^2_0(\Omega)$ such that

$$a(\{u, \boldsymbol{\zeta}\}, \{\delta u, \delta\boldsymbol{\zeta}\}) + b(\{\delta u, \delta\boldsymbol{\zeta}\}, m) = d(\{\delta u, \delta\boldsymbol{\zeta}\}) \quad \text{for all } \{\delta u, \delta\boldsymbol{\zeta}\} \in X\,, \tag{3.15a}$$

$$b(\{u, \boldsymbol{\zeta}\}, \delta m) - \frac{1}{\mu_{macro}\,L_c^2}c(m, \delta m) = 0 \quad \text{for all } \delta m \in L^2_0(\Omega)\,, \tag{3.15b}$$

where the Lagrange multiplier m has the physical meaning of a moment stress tensor.

The limit case $\lim L_c \to \infty$ of Eq. (3.15) is well-defined, resulting in the problem: Find $(\{u_\infty, \boldsymbol{\zeta}_\infty\}, m_\infty) \in X \times L^2_0(\Omega)$

such that

$$a(\{u_\infty, \boldsymbol{\zeta}_\infty\}, \{\delta u, \delta\boldsymbol{\zeta}\}) + b(\{\delta u, \delta\boldsymbol{\zeta}\}, m_\infty) = d(\{\delta u, \delta\boldsymbol{\zeta}\}) \qquad \text{for all } \{\delta u, \delta\boldsymbol{\zeta}\} \in X\,, \tag{3.16a}$$

$$b(\{u_\infty, \boldsymbol{\zeta}_\infty\}, \delta m) = 0 \qquad \text{for all } \delta m \in L^2_0(\Omega)\,. \tag{3.16b}$$

Consequently, at the limit $\lim L_c \to \infty$ we have $\operatorname{curl}_{2D} \boldsymbol{\zeta} = 0$.

We now show existence and uniqueness of both mixed problems and that in the limit case $L_c \to \infty$ the solution of Eq. (3.15) converges to the solution of Eq. (3.16) with quadratic convergence rate in L_c.

Theorem 3.4 *For $\mu_e, \mu_{micro}, \mu_{macro}, L_c > 0$ Eq. (3.15) has a unique solution $(\{u, \boldsymbol{\zeta}\}, m) \in X \times L^2_0(\Omega)$ satisfying for $(\mu_{macro} L_c^2)^{-1} \leq 1$ the stability estimate*

$$\|\{u, \boldsymbol{\zeta}\}\|_X + \|m\|_{L^2} \leq c_1 \Big(\|f\|_{L^2} + \|\boldsymbol{\omega}\|_{L^2} \Big)\,, \tag{3.17}$$

where c_1 is independent of L_c. Further, let $(\{u_\infty, \boldsymbol{\zeta}_\infty\}, m_\infty) \in X \times L^2_0(\Omega)$ be the unique solution of Eq. (3.16). Then, we have the estimate

$$\|\{u_\infty - u, \boldsymbol{\zeta}_\infty - \boldsymbol{\zeta}\}\|_X + \|m_\infty - m\|_{L^2} \leq \frac{c_2}{L_c^2} \Big(\|f\|_{L^2} + \|\boldsymbol{\omega}\|_{L^2} \Big)\,, \tag{3.18}$$

where c_2 does not depend on L_c.

Proof Existence and uniqueness follows from the extended Brezzi theorem [6, Thm. 4.11]. The continuity of $a(\cdot,\cdot)$, $b(\cdot,\cdot)$, $c(\cdot,\cdot)$ and non-negativity of $a(\cdot,\cdot)$ and $c(\cdot,\cdot)$ are obvious. Therefore, we have to prove that $a(\cdot,\cdot)$ is coercive on the kernel of $b(\cdot,\cdot)$

$$\begin{aligned} \ker(b) &= \Big\{ \{u, \boldsymbol{\zeta}\} \in X \mid b(\{u, \boldsymbol{\zeta}\}, \delta m) = 0 \ \text{ for all } \delta m \in L^2_0(\Omega) \Big\} \\ &= \Big\{ \{u, \boldsymbol{\zeta}\} \in X \mid \operatorname{curl}_{2D} \boldsymbol{\zeta} = 0 \Big\}\,. \end{aligned} \tag{3.19}$$

However, we already know from Theorem 3.1 that $a(\{u, \boldsymbol{\zeta}\}, \{\delta u, \delta\boldsymbol{\zeta}\}) + \int_\Omega \langle \operatorname{curl}_{2D} \boldsymbol{\zeta}, \operatorname{curl}_{2D} \delta\boldsymbol{\zeta} \rangle \, dX$ is coercive. This leaves us with the Ladyzhenskaya–Babuška–Brezzi (LBB) condition to be satisfied

$$\exists\, \beta_2 > 0 : \quad \sup_{\{u,\boldsymbol{\zeta}\} \in X} \frac{b(\{u, \boldsymbol{\zeta}\}, m)}{\|\{u, \boldsymbol{\zeta}\}\|_X} \geq \beta_2 \, \|m\|_{L^2} \quad \text{for all } m \in L^2_0(\Omega)\,. \tag{3.20}$$

We choose $u = 0$ and $\boldsymbol{\zeta}$ such that $\operatorname{curl}_{2D} \boldsymbol{\zeta} = m$ with $\|\boldsymbol{\zeta}\|_{L^2} \leq c \|m\|_{L^2}$ leading to

$$\frac{b(\{u, \boldsymbol{\zeta}\}, m)}{\|\{u, \boldsymbol{\zeta}\}\|_X} = \frac{\int_\Omega \langle m, \operatorname{curl}_{2D} \boldsymbol{\zeta} \rangle \, dX}{\|\boldsymbol{\zeta}\|_{L^2} + \|\operatorname{curl}_{2D} \boldsymbol{\zeta}\|_{L^2}} \geq c \, \frac{\|m\|^2_{L^2}}{\|m\|_{L^2}} = c \, \|m\|_{L^2}\,, \tag{3.21}$$

where the construction of $\boldsymbol{\zeta}$ is according to [18][4]. Thus, there exists a unique solution independent of L_c satisfying the stability estimate Eq. (3.17).

With the (classical) Brezzi-Theorem also the existence and uniqueness of Eq. (3.16) follows immediately and estimate Eq. (3.18) due to the continuous dependence of the solution with respect to the parameter L_c, [6, Cor. 4.15]. □

Remark 3.4 As mentioned in [18] the space for m must be chosen as $L^2_0(\Omega)$, where its mean is zero, if Dirichlet data are prescribed on the whole boundary $\Gamma^\zeta_D = \partial\Omega$. This follows from Eq. (3.13)

$$\begin{aligned} \int_\Omega m \, dX &= \mu_{macro} L_c^2 \int_\Omega \operatorname{curl}_{2D} \boldsymbol{\zeta} \, dX \\ &= \mu_{macro} L_c^2 \int_{\partial\Omega} \langle \boldsymbol{\zeta}, \boldsymbol{\tau} \rangle \, ds = 0 \qquad \text{for all } \boldsymbol{\zeta} \in H_0(\operatorname{curl}, \Omega). \end{aligned} \tag{3.22}$$

If also Neumann data is prescribed for $\boldsymbol{\zeta}$, the appropriate function space for m is $L^2(\Omega)$.

Remark 3.5 In the full micromorphic continuum, where the gradient takes the place of the curl of the microdistortion

$$\underbrace{\int_\Omega 2\mu_e \langle (\nabla u - \boldsymbol{\zeta}), (\nabla \delta u - \delta\boldsymbol{\zeta}) \rangle + 2\mu_{micro} \langle \boldsymbol{\zeta}, \delta\boldsymbol{\zeta} \rangle + \mu_{macro} L_c^2 \langle \nabla\boldsymbol{\zeta}, \nabla\delta\boldsymbol{\zeta} \rangle \, dX}_{= a_{grad}(\{u, \boldsymbol{\zeta}\}, \{\delta u, \delta\boldsymbol{\zeta}\})} = \int_\Omega \langle \delta u, f \rangle + \langle \delta\boldsymbol{\zeta}, \boldsymbol{\omega} \rangle \, dX\,, \tag{3.23}$$

[4] The construction is derived directly from the 2D Stokes LBB condition with $H(\mathrm{div})$-conforming elements and applies here since the curl_{2D} operator is a rotated divergence operator in two dimensions.

existence and uniqueness follow similarly with the space $X = H^1(\Omega) \times [H^1(\Omega)]^2$. However, the limit case $L_c \to \infty$ yields $\nabla\boldsymbol{\zeta} = 0$ and consequently $\boldsymbol{\zeta} = const.$, for which non-trivial boundary conditions cannot be considered, compare also Section 5.7 for a numerical example.

To conclude this section we investigate the necessary and sufficient conditions such that in the limit $L_c \to \infty$ the solution satisfies $\nabla u = \boldsymbol{\zeta}$. This state represents a zoom into the microstructure in the three-dimensional theory with microscopic stiffness given by μ_{micro} [29]. In Theorem 3.2 we found sufficient conditions to obtain a gradient field for the microdistortion, which, however, does not have to be ∇u. The following theorem states that only for a zero right-hand side f, but arbitrary $\boldsymbol{\omega}$, the desired behaviour is achieved.

Theorem 3.5 *Let Ω be simply connected and $\Gamma_D^u = \Gamma_D^\zeta = \partial\Omega$. Then there holds for the solution $\{u, \boldsymbol{\zeta}\} \in X$ of Problem 3.4*

$$\|\boldsymbol{\zeta} - \nabla u\|_{H(\text{curl})} \leq \frac{c}{L_c^2}\,, \tag{3.24}$$

if and only if $f = 0$, where c does not depend on L_c.

Proof From the limit solution $\{u_\infty, \boldsymbol{\zeta}_\infty\} \in X$ of Eq. (3.16) we have that $\boldsymbol{\zeta}_\infty \in H_0(\text{curl}, \Omega)$ and $\text{curl}_{2D}\,\boldsymbol{\zeta}_\infty = 0$. This implies the existence of $\Psi \in H_0^1(\Omega)$ such that $\boldsymbol{\zeta} = \nabla\Psi \in \ker(\text{curl}_{2D})$. Inserting this into Eq. (3.16a), where $\delta\boldsymbol{\zeta} = 0$ is chosen, yields

$$\int_\Omega 2\mu_e \langle \nabla u - \nabla\Psi, \nabla\delta u\rangle \,\mathrm{d}X = \int_\Omega \langle \delta u,\ f\rangle \,\mathrm{d}X$$
$$\text{for all } \delta u \in H_0^1(\Omega).$$

Thus, $u = \Psi \in H_0^1(\Omega)$ is the unique solution if and only if $f = 0$ and correspondingly $\{u_\infty, \boldsymbol{\zeta}_\infty\} = \{\Psi, \nabla\Psi\}$. The claim follows with the triangle inequality, Eq. (3.18) and the equivalence of the mixed and primal problem

$$\|\boldsymbol{\zeta} - \nabla u\|_{H(\text{curl})} \leq \|\boldsymbol{\zeta} - \boldsymbol{\zeta}_\infty\|_{H(\text{curl})} + \|\underbrace{\boldsymbol{\zeta}_\infty - \nabla u_\infty}_{=0}\|_{H(\text{curl})}$$
$$+\|\nabla u_\infty - \nabla u\|_{L^2} \leq \frac{c}{L_c^2}\,.$$

□

Remark 3.6 We can weaken the assumptions of Theorem 3.5 to $\Gamma_D^u = \Gamma_D^\zeta \neq \emptyset$. Further, also non-homogeneous Dirichlet data can be considered, provided the consistent coupling condition $\langle \boldsymbol{\zeta},\ \boldsymbol{\tau}\rangle = \langle \nabla\widetilde{u},\ \boldsymbol{\tau}\rangle$ on Γ_D^ζ holds.

From the proof of Theorem 3.5 we obtain from the existence of a potential such that $\boldsymbol{\zeta} = \nabla\Psi$. Thus, $\boldsymbol{\zeta}$ is expected to be in $H(\text{curl}, \Omega)$ as in general $\nabla\Psi \notin [H^1(\Omega)]^2$ for $\Psi \in H^1(\Omega)$.

3.2 Discrete case

Motivated by the de' Rham complex (see Fig. 2) we formulate a finite element combining base functions from both $H^1(\Omega)$ and $H(\text{curl}, \Omega)$ (and $L^2(\Omega)$ for the mixed formulation) setting

$$u^h,\ \delta u^h \in V^h \subset H^1(\Omega)\,,\quad \boldsymbol{\zeta}^h,\ \delta\boldsymbol{\zeta}^h \in U^h \subset H(\text{curl}, \Omega)\,,$$
$$m^h, \delta m^h \in Q^h \subset L^2(\Omega)\,. \tag{3.25}$$

Throughout this work we will use meshes consisting of quadrilaterals. On each element we denote the set of quadrilateral polynomials by $Q^{n,m} = \text{span}\{x^k y^j \mid 0 \leq k \leq n,\ 0 \leq j \leq m\}$, compare also Eq. (4.5), and further the set of Nédélec ansatz functions by

$$P^k = \begin{bmatrix} Q^{k-1,k} \\ Q^{k,k-1} \end{bmatrix}. \tag{3.26}$$

We start with the Lax–Milgram setting by defining $X^h = V^h \times U^h$. We note that solvability of the discretized problem follows directly from the continuous one as $X^h \subset X$. Using Cea's lemma for the quasi-best approximation

$$\|\{u, \boldsymbol{\zeta}\} - \{u^h, \boldsymbol{\zeta}^h\}\|_X \leq \frac{\alpha}{\beta} \inf_{\{\delta u^h, \delta\boldsymbol{\zeta}^h\} \in X^h} \|\{u, \boldsymbol{\zeta}\} - \{\delta u^h, \delta\boldsymbol{\zeta}^h\}\|_X\,, \tag{3.27}$$

we can generate convergence estimates a priori.

Lemma 3.1 *Assume a smooth exact solution $\{u, \boldsymbol{\zeta}\} \in X$. Further, if on each element $Q^{k,k} \subset V^h$ and $P^k \subset U^h$, then the discrete solution $\{u^h, \boldsymbol{\zeta}^h\} \in X^h$ converges with the optimal convergence rate*

$$\|\{u, \boldsymbol{\zeta}\} - \{u^h, \boldsymbol{\zeta}^h\}\|_X \leq c(L_c^2, \mu_e, \mu_{\text{micro}}, \mu_{\text{macro}})\, h^k\,. \tag{3.28}$$

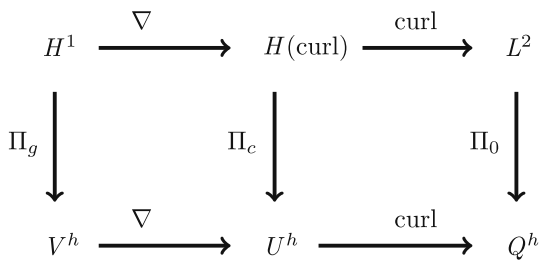

Fig. 2 The de' Rham complex in two dimensions depicting Hilbert spaces and approximation spaces connected by differential and interpolation operators. The kernel of one differential operator is exactly the range of the previous differential operator on its space and the differential and projection operators commute

Proof By inserting the interpolation operators associated through the commuting diagram we find

$$\begin{aligned}
\|\{u,\boldsymbol{\zeta}\}-\{u^h,\boldsymbol{\zeta}^h\}\|_X^2 &\le c \inf_{\{\delta u^h,\delta\boldsymbol{\zeta}^h\}\in X^h} \|\{u,\boldsymbol{\zeta}\}-\{\delta u^h,\delta\boldsymbol{\zeta}^h\}\|_X^2 \\
&\le c\Big(\|u-\Pi_g u\|_{H^1}^2 + \|\boldsymbol{\zeta}-\Pi_c\boldsymbol{\zeta}\|_{L^2}^2 \\
&\quad + \|\operatorname{curl}_{2\mathrm{D}}\boldsymbol{\zeta}-\operatorname{curl}_{2\mathrm{D}}\Pi_c\boldsymbol{\zeta}\|_{L^2}^2\Big) \\
&= c\Big(\|u-\Pi_g u\|_{H^1}^2 + \|\boldsymbol{\zeta}-\Pi_c\boldsymbol{\zeta}\|_{L^2}^2 \\
&\quad + \|(\mathrm{id}-\Pi_0)\operatorname{curl}_{2\mathrm{D}}\boldsymbol{\zeta}\|_{L^2}^2\Big) \\
&\le c\,h^{2k}\Big(|u|_{H^{k+1}}^2 + |\boldsymbol{\zeta}|_{H^k}^2 + |\operatorname{curl}_{2\mathrm{D}}\boldsymbol{\zeta}|_{H^k}^2\Big), \qquad (3.29)
\end{aligned}$$

where $|\cdot|_{H^k}$ denotes the standard Sobolev semi-norm. □

Note that the constant c in Eq. (3.28) depends on L_c. One may prove robust estimates in this setting. We, however, test for robustness with respect to L_c in the context of mixed methods and use the equivalence of both.

In general the solvability of the discretized mixed problem does not follow from the continuous one. However, thanks to the commuting property of the de' Rham complex, the discrete kernel coercivity and the LBB condition follow immediately. Thus, we obtain the quasi-best approximation error

$$\begin{aligned}
&\|\{u,\boldsymbol{\zeta}\}-\{u^h,\boldsymbol{\zeta}^h\}\|_X + \|m-m^h\|_{L^2} \\
&\quad\le c \inf_{(\{\delta u^h,\delta\boldsymbol{\zeta}^h\},\delta\omega^h)\in X^h\times Q^h} \Big(\|\{u,\boldsymbol{\zeta}\}-\{\delta u^h,\delta\boldsymbol{\zeta}^h\}\|_X \\
&\qquad + \|m-\delta m^h\|_{L^2}\Big), \qquad (3.30)
\end{aligned}$$

where c is independent of L_c.

Lemma 3.2 *Assume that the exact solution $(\{u,\boldsymbol{\zeta}\},m)\in X\times L^2(\Omega)$ of Eq. (3.15) is smooth and that on each element $Q^{k,k}\subset V^h$, $P^k\subset U^h$, and $Q^{k-1,k-1}\subset Q^h$. Then the discrete solution $(\{u^h,\boldsymbol{\zeta}^h\},m^h)\in X_h\times Q_h$ satisfies the optimal convergence rate independent of L_c*

$$\|\{u,\boldsymbol{\zeta}\}-\{u^h,\boldsymbol{\zeta}^h\}\|_X + \|m-m^h\|_{L^2} \le c\,h^k. \qquad (3.31)$$

Additionally, with $\{u_\infty,\boldsymbol{\zeta}_\infty\}$ the (smooth) solution of the limit problem we obtain

$$\|\{u_\infty,\boldsymbol{\zeta}_\infty\}-\{u^h,\boldsymbol{\zeta}^h\}\|_X + \|m_\infty-m^h\|_{L^2} \le \frac{c_1}{L_c^2} + c_2\,h^k. \qquad (3.32)$$

Proof Using the interpolation operators Π_g, Π_c, and Π_0 gives estimate Eq. (3.31). Inequality Eq. (3.32) follows immediately by adding and subtracting the solution of the corresponding continuous solution $(\{u,\boldsymbol{\zeta}\},m)\in X\times L^2(\Omega)$ for a fixed L_c, using triangle inequality, Eq. (3.18) and Eq. (3.31). □

Inequality Eq. (3.32) states that, as long as the discretization error is not reached, we have quadratic convergence to the limit case $\lim L_c\to\infty$. Due to the equivalence of the primal formulation Problem 3.4 and the mixed Eq. (3.15) we can deduce that the solution of Problem 3.4 is also robust with respect to L_c. As we will see in the numerical examples, the mixed formulation is better suited for extremely large values of L_c due to rounding errors.

4 Finite element formulations

4.1 Appropriate base functions

In the following we demonstrate the construction of the hybrid element in the linear case. The finite elements for the mixed formulation are employed directly using the open source finite element library NETGEN/NGSolve[5] [39,40].

For the mapping of x and y, see Fig. 3, we make use of linear quadrilateral Lagrange nodal base functions

$$\begin{aligned}
N_1(\xi,\eta) &= \frac{1}{4}(\xi-1)(\eta-1), \\
N_2(\xi,\eta) &= \frac{1}{4}(\xi+1)(1-\eta), \\
N_3(\xi,\eta) &= \frac{1}{4}(\xi+1)(\eta+1), \\
N_4(\xi,\eta) &= \frac{1}{4}(1-\xi)(\eta+1), \qquad (4.1)
\end{aligned}$$

$$x = \bigcup_{e=1}^{n} \underbrace{\begin{bmatrix}N_1 & N_2 & N_3 & N_4\end{bmatrix}}_{\boldsymbol{H}(\xi,\eta)} \underbrace{\begin{bmatrix}x_1\\x_2\\x_3\\x_4\end{bmatrix}}_{\bar{\mathbf{x}}_e}, \qquad y = \bigcup_{e=1}^{n} \boldsymbol{H}\mathbf{y}_e,$$

$$\mathbf{x} = \begin{bmatrix}x & y\end{bmatrix}^T, \qquad (4.2)$$

where n is the number of finite elements in the mesh. As shown in Fig. 3, the elements are mapped via

$$\begin{aligned}
&\mathbf{x}:\Xi\mapsto\Omega, \qquad \Xi=[-1,1]\times[-1,1], \\
&\Omega = \bigcup_{e=1}^{n}\Omega_e\subset\mathbb{R}^2. \qquad (4.3)
\end{aligned}$$

We approximate u according to the isoparametric concept

$$u_e^h = \boldsymbol{H}\bar{\mathbf{u}}_e, \qquad u^h = \bigcup_{e=1}^{n} u_e^h. \qquad (4.4)$$

[5] www.ngsolve.org

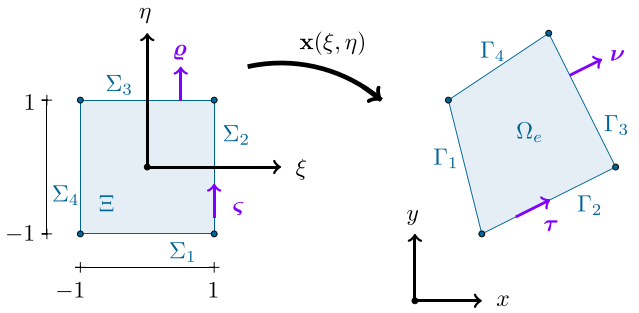

Fig. 3 Element mapping from the parametric space into the physical space

However, for $\boldsymbol{\zeta}$ we make use of linear Nédélec base functions of the first type for quadrilaterals [4,21,27,44]. These functions are built around approximations of the curl operator. The corresponding spaces are those of quadrilateral polynomials

$$p(\xi,\eta) = \left(\sum_{k=0}^{n} c_k \xi^k\right)\left(\sum_{j=0}^{m} d_j \eta^j\right) \in Q^{n,m} \,. \tag{4.5}$$

The weak form of the curl in the 2D space is formulated via Greens' formula[6]

$$\int_\Omega q \ \mathrm{curl}_{2\mathrm{D}}\, \boldsymbol{\zeta}\, \mathrm{d}X = \oint_{\partial\Omega} \langle q\, \boldsymbol{\zeta},\, \boldsymbol{\tau}\rangle\, \mathrm{d}s + \int_\Omega \langle \boldsymbol{\zeta},\, \mathrm{D}^{\mathrm{curl}}\, q\rangle\, \mathrm{d}X$$
$$\text{for all } q \in C^1(\Omega,\, \mathbb{R})\,. \tag{4.6}$$

Therefore, the curl in Ω is fully determined by its interface and inner rotation field. Consequently, we can decompose the two terms, such that the elements' dofs determine the interpolated field completely. This can be confirmed by setting all dofs to zero, checking for a vanishing field. The corresponding dofs and degrees of the polynomial spaces have been defined by Nédélec [27]. The element's boundary has been decomposed as $\partial\,\Xi = \Sigma_1 \cup \Sigma_2 \cup \Sigma_3 \cup \Sigma_4$. The dofs read

$$4k \text{ edge dofs:} \qquad f_{ij}(\boldsymbol{\vartheta}) = \int_{\Sigma_j} q_i\, \langle\, \boldsymbol{\vartheta},\, \boldsymbol{\varsigma}_j\rangle\, \mathrm{d}\Sigma$$
$$\boldsymbol{\vartheta} \in P^k(\Xi) \quad \text{for all } q_i \in \mathbb{P}^{k-1}(\Sigma_j)\,,$$
$$2k(k-1) \text{ cell dofs:} \quad f_i(\boldsymbol{\vartheta}) = \int_\Xi \langle \boldsymbol{\vartheta},\, \mathbf{q}_i\rangle\, \mathrm{d}\,\Xi\,,$$
$$\boldsymbol{\vartheta} \in P^k(\Xi) \quad \text{for all } \mathbf{q}_i = \begin{bmatrix} q_1 \\ q_2 \end{bmatrix},\ \begin{matrix} q_1 \in Q^{k-2,k-1}(\Xi) \\ q_2 \in Q^{k-1,k-2}(\Xi) \end{matrix}, \tag{4.7}$$

[6] $\mathrm{curl}_{2\mathrm{D}}(q\,\boldsymbol{\zeta}) = \mathrm{div}(\boldsymbol{R}\,(q\,\boldsymbol{\zeta})) = q\ \mathrm{curl}_{2\mathrm{D}}\,\boldsymbol{\zeta} - \langle \boldsymbol{\zeta},\, \mathrm{D}^{\mathrm{curl}}\, q\rangle\,, \quad \boldsymbol{R} = \begin{bmatrix} 0 & 1 \\ -1 & 0 \end{bmatrix}$.

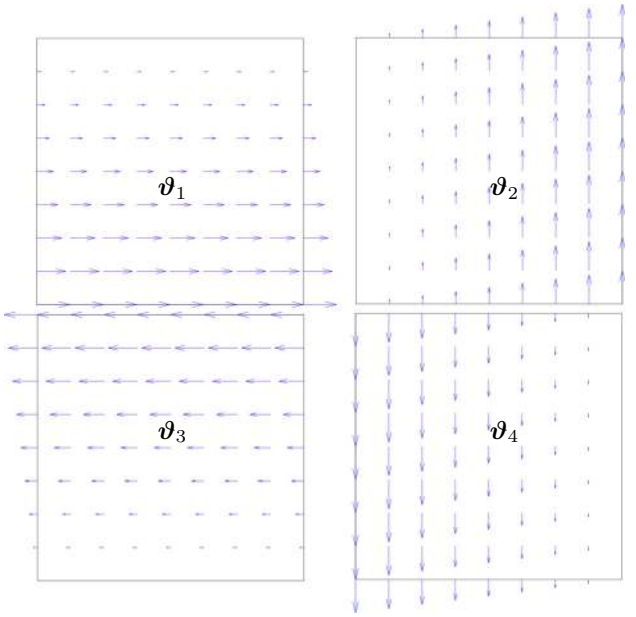

Fig. 4 Nédélec base functions from Eq. (4.10) in the parametric space

where P^k and Q are according to Eq. (3.26) and Eq. (4.5), and $\mathbb{P}^k$ is the space of polynomials of order k. Since we employ linear Nédélec base functions with $k = 1$, no inner dofs occur. The ansatz for the base function reads

$$\boldsymbol{\vartheta}_m(\xi,\eta) = \begin{bmatrix} d_0 + d_1\eta \\ c_0 + c_1\xi \end{bmatrix}, \qquad \boldsymbol{\vartheta}_m(\xi,\eta) \in P^1(\Xi)\,,$$
$$m = \Big\{1,\, 2,\, \ldots,\, \dim(P^1) = 4\Big\}\,. \tag{4.8}$$

Applying the dofs along all edges with the variable basis $q_i = 1$

$$f_{ij}(\boldsymbol{\vartheta}_m) = \int_{\Sigma_j} q_i\, \langle \boldsymbol{\vartheta}_m,\, \boldsymbol{\varsigma}_j\rangle\, \mathrm{d}\Sigma = \delta_{ij}\,, \tag{4.9}$$

we find our base functions

$$\boldsymbol{\vartheta}_1 = \frac{1}{2}\begin{bmatrix} 1-\eta \\ 0 \end{bmatrix}, \qquad \boldsymbol{\vartheta}_2 = \frac{1}{2}\begin{bmatrix} 0 \\ 1+\xi \end{bmatrix},$$
$$\boldsymbol{\vartheta}_3 = \frac{1}{2}\begin{bmatrix} -1-\eta \\ 0 \end{bmatrix}, \qquad \boldsymbol{\vartheta}_4 = \frac{1}{2}\begin{bmatrix} 0 \\ \xi-1 \end{bmatrix}. \tag{4.10}$$

The factor $1/2$ is chosen instead of the resulting $1/4$ as to simplify prescription on the Dirichlet boundary. The functions are depicted in Fig. 4.

For the mixed formulation involving $m \in L^2(\Omega)$ the corresponding finite element space is given by piece-wise constants, $N_0(\xi,\eta) = 1$. To enforce zero mean value, i.e. $m \in L^2_0(\Omega)$, a Lagrange multiplier $\lambda \in \mathbb{R}$ has to be used, leading to one additional equation in the final system.

Using higher polynomial orders, we can achieve faster convergence rates and better approximations. The finite element software NGSolve offers the use of hierarchical high order base functions for H^1, $H(\mathrm{curl})$, and L^2 spaces [44]. We employ NGSolve in our investigation of the mixed formulation with higher order base functions.

4.2 Covariant Piola transformation

In the previous section we formulated our base functions for the curl in the parametric space. In order to preserve the properties of the base function $\boldsymbol{\vartheta}_j$ acting on the curve's tangents $\boldsymbol{\varsigma}$ (see Fig. 3), namely

$$\int_{\Sigma_i} \langle \boldsymbol{\vartheta}_j,\ \boldsymbol{\varsigma} \rangle \,\mathrm{d}\Sigma = \int_{\Gamma_i} \langle \boldsymbol{\theta}_j,\ \boldsymbol{\tau} \rangle \,\mathrm{d}s = \delta_{ij}\,, \tag{4.11}$$

where $\boldsymbol{\theta}_j$ is the base function in the physical space and $\partial\Omega_e = \Gamma_1 \cup \Gamma_2 \cup \Gamma_3 \cup \Gamma_4$, the so called covariant Piola transformation is required [24]. The transformation is achieved by considering the push forward of the boundaries' normal vectors

$$\langle \mathbf{v},\ \boldsymbol{\nu} \rangle = \det \boldsymbol{J}\, \langle \mathbf{v},\ \boldsymbol{J}^{-T} \boldsymbol{\varrho} \rangle\,, \tag{4.12}$$

where $\boldsymbol{J}$ is the Jacobi matrix of the element mappings. In two dimensions the normal vectors on the element boundary $\boldsymbol{\varrho}$ and $\boldsymbol{\nu}$ are the 90° rotation of the tangent vectors given by

$$\boldsymbol{\varrho} = \boldsymbol{R}\boldsymbol{\varsigma}\,, \qquad \boldsymbol{\nu} = \boldsymbol{R}\boldsymbol{\tau}\,, \qquad \boldsymbol{R} = \begin{bmatrix} 0 & 1 \\ -1 & 0 \end{bmatrix}. \tag{4.13}$$

Using Eq. (4.13) in Eq. (4.12) results in

$$\langle \mathbf{v},\ \boldsymbol{R}\boldsymbol{\tau} \rangle = \det \boldsymbol{J}\, \langle \mathbf{v},\ \boldsymbol{J}^{-T} \boldsymbol{R}\boldsymbol{\varsigma} \rangle\,, \tag{4.14}$$

finally yielding the definition of a transformation preserving integration along the tangent

$$\mathbf{v}_0 = \det \boldsymbol{J}\, \boldsymbol{R}^T \boldsymbol{J}^{-1} \boldsymbol{R}\, \mathbf{v}\,, \qquad \mathbf{v} = \underbrace{\frac{1}{\det \boldsymbol{J}}\, \boldsymbol{R}^T \boldsymbol{J} \boldsymbol{R}}_{\boldsymbol{J}^{-T}}\, \mathbf{v}_0\,. \tag{4.15}$$

The transformation in Eq. (4.15) alone cannot guarantee the aligned orientation of base functions on the edges of neighbouring elements [44]. In order to achieve conformity we introduce a topological correction function ψ_j based on the global orientation of edges given by node collections as demonstrated in Fig. 5. The drawings in Fig. 5 show the different roles of the mapping functions:

1. The covariant Piola transformation scales the projection onto the edge tangent.
2. The topological correction function sets a consistent orientation.

Thus, the final form of our edge base functions reads

$$\boldsymbol{\theta}_j = \psi_j \boldsymbol{J}^{-T} \boldsymbol{\theta}_j\,, \qquad \psi_j = \begin{cases} 1 & \text{orientation is equal} \\ -1 & \text{else} \end{cases} \tag{4.16}$$

Using Eq. (4.16) for the approximation of the microdistortion $\boldsymbol{\zeta}$ yields

$$\boldsymbol{\zeta}_e^h = \underbrace{[\boldsymbol{\theta}_1\ \boldsymbol{\theta}_2\ \boldsymbol{\theta}_3\ \boldsymbol{\theta}_4]}_{\boldsymbol{\Theta}} \underbrace{\begin{bmatrix} \zeta_1 \\ \zeta_2 \\ \zeta_3 \\ \zeta_4 \end{bmatrix}}_{\bar{\boldsymbol{\zeta}}_e}, \qquad \boldsymbol{\zeta}^h = \bigcup_{e=1}^{n} \boldsymbol{\zeta}_e^h\,. \tag{4.17}$$

For vectors undergoing a covariant Piola transformation, the transformation of the curl operator simplifies to

$$\mathrm{curl}_{2\mathrm{D}_x} \boldsymbol{\theta}_j = \frac{1}{\det \boldsymbol{J}} \psi_j \,\mathrm{curl}_{2\mathrm{D}}\, \boldsymbol{\theta}_j\,. \tag{4.18}$$

4.3 Element stiffness matrices

For ease of presentation we consider only the Lax–Milgram setting. The mixed formulation follows directly with simple adaptations.

With the approximations in Eq. (4.4) for the displacement field u and in Eq. (4.17) for the microdistortion $\boldsymbol{\zeta}$ the weak form in Problem 3.4 results in

$$\bigcup_{e=1}^{n} (\boldsymbol{K}_{\mathrm{e}} + \boldsymbol{K}_{\mathrm{micro}} + \boldsymbol{K}_{\mathrm{macro}})_e \begin{bmatrix} \bar{\mathbf{u}}_e \\ \bar{\boldsymbol{\zeta}}_e \end{bmatrix} = \bigcup_{e=1}^{n} \begin{bmatrix} \bar{\mathbf{f}}_e \\ \bar{\boldsymbol{\omega}}_e \end{bmatrix}, \tag{4.19}$$

where $\boldsymbol{K}_{\mathrm{e}}$, $\boldsymbol{K}_{\mathrm{micro}}$ and $\boldsymbol{K}_{\mathrm{macro}}$ are the element stiffness matrices employing the base function matrices $\boldsymbol{H}$ and $\boldsymbol{\Theta}$ according to Eq. (4.17) and Eq. (4.2), respectively

$$\boldsymbol{K}_{\mathrm{e}} = 2\mu_{\mathrm{e}} \int_{\Xi} \begin{bmatrix} (\nabla \boldsymbol{H})^T \nabla \boldsymbol{H} & -(\nabla \boldsymbol{H})^T \boldsymbol{\Theta} \\ -\boldsymbol{\Theta}^T \nabla \boldsymbol{H} & \boldsymbol{\Theta}^T \boldsymbol{\Theta} \end{bmatrix} \det \boldsymbol{J}\,\mathrm{d}\Xi\,, \tag{4.20a}$$

$$\boldsymbol{K}_{\mathrm{micro}} = 2\mu_{\mathrm{micro}} \int_{\Xi} \begin{bmatrix} \boldsymbol{O} & \boldsymbol{O} \\ \boldsymbol{O} & \boldsymbol{\Theta}^T \boldsymbol{\Theta} \end{bmatrix} \det \boldsymbol{J}\,\mathrm{d}\Xi\,, \tag{4.20b}$$

$$\boldsymbol{K}_{\mathrm{macro}} = \mu_{\mathrm{macro}} L_{\mathrm{c}}^2 \int_{\Xi} \begin{bmatrix} \boldsymbol{O} & \boldsymbol{O} \\ \boldsymbol{O} & (\mathrm{curl}_{2\mathrm{D}}\, \boldsymbol{\Theta})^T \,\mathrm{curl}_{2\mathrm{D}}\, \boldsymbol{\Theta} \end{bmatrix} \det \boldsymbol{J}\,\mathrm{d}\Xi\,, \tag{4.20c}$$

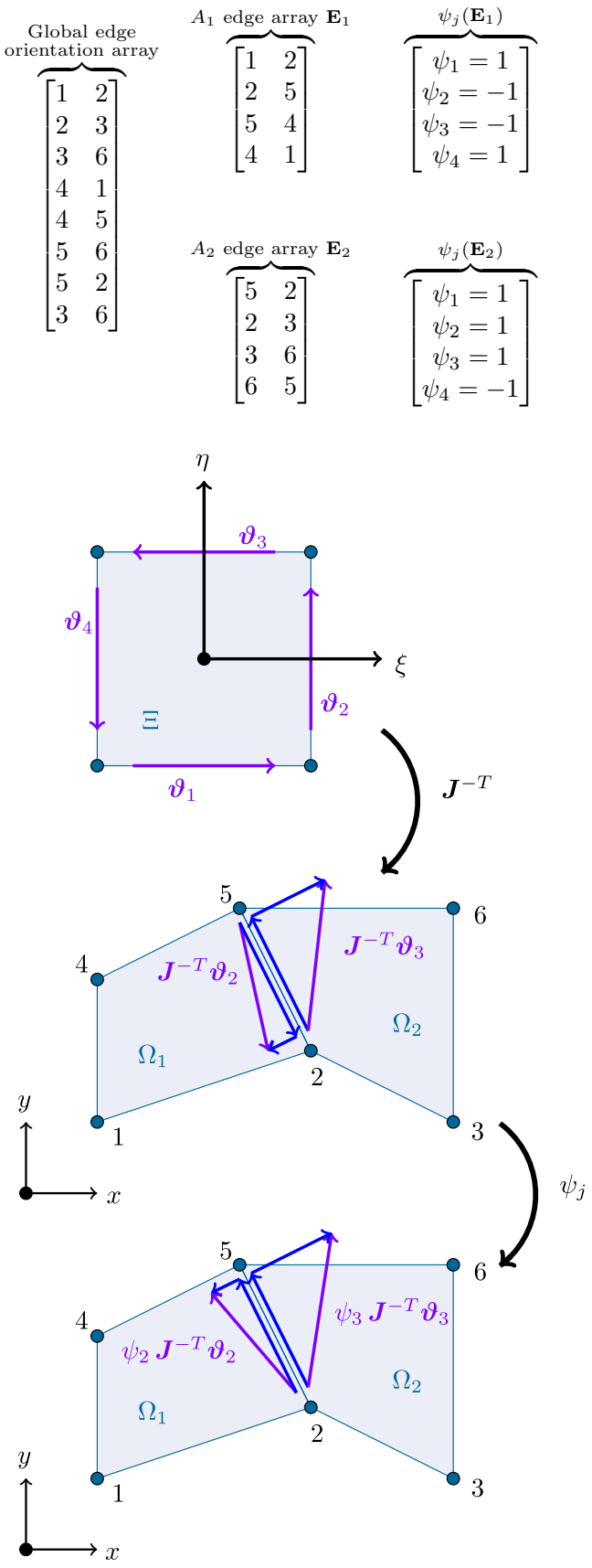

Fig. 5 Covariant Piola transformation and topological correction function ψ_j mapping of Nédélec base functions from the parametric space into the physical space

with $\boldsymbol{O} \in \{0\}^{4\times4}$. The finite element has 8 degrees of freedom. The right-hand side reads

$$\bar{\mathbf{f}}_e = \int_\Xi \boldsymbol{H}^T f \det \boldsymbol{J}\, \mathrm{d}\Xi\,, \tag{4.21}$$

$$\bar{\boldsymbol{\omega}}_e = \int_\Xi \boldsymbol{\Theta}^T \boldsymbol{\omega} \det \boldsymbol{J}\, \mathrm{d}\Xi\,. \tag{4.22}$$

In order to compare our formulation, we also derive a nodal H^1-finite element

$$\boldsymbol{\zeta} = \bigcup_{e=1}^{n} \underbrace{\begin{bmatrix} N_1\boldsymbol{I} & N_2\boldsymbol{I} & N_3\boldsymbol{I} & N_4\boldsymbol{I}\end{bmatrix}}_{\boldsymbol{N}} \underbrace{\begin{bmatrix}\zeta_1\\ \zeta_2\\ \vdots\\ \zeta_8\end{bmatrix}}_{\bar{\boldsymbol{\zeta}}_e}, \quad \boldsymbol{I} = \begin{bmatrix}1&0\\0&1\end{bmatrix}. \tag{4.23}$$

In contrast to the hybrid element, the approach in Eq. (4.23) requires 8 dofs per element for the microdistortion. Using Eq. (4.23) we obtain the following stiffness matrices for the nodal element

$$\boldsymbol{K}_\mathrm{e} = 2\mu_\mathrm{e} \int_\Omega \begin{bmatrix} (\nabla\boldsymbol{H})^T\nabla\boldsymbol{H} & -(\nabla\boldsymbol{H})^T\boldsymbol{N} \\ -\boldsymbol{N}^T\nabla\boldsymbol{H} & \boldsymbol{N}^T\boldsymbol{N}\end{bmatrix} \det\boldsymbol{J}\,\mathrm{d}\Omega\,, \tag{4.24a}$$

$$\boldsymbol{K}_\mathrm{micro} = 2\mu_\mathrm{micro} \int_\Omega \begin{bmatrix} \boldsymbol{O} & \boldsymbol{O}_\mathrm{a}^T \\ \boldsymbol{O}_\mathrm{a} & \boldsymbol{N}^T\boldsymbol{N}\end{bmatrix} \det\boldsymbol{J}\,\mathrm{d}\Omega\,, \tag{4.24b}$$

$$\boldsymbol{K}_\mathrm{macro} = \mu_\mathrm{macro} L_\mathrm{c}^2 \int_\Omega \begin{bmatrix} \boldsymbol{O} & \boldsymbol{O}_\mathrm{a}^T \\ \boldsymbol{O}_\mathrm{a} & (\mathrm{curl_{2D}}\,\boldsymbol{N})^T\,\mathrm{curl_{2D}}\,\boldsymbol{N}\end{bmatrix} \det\boldsymbol{J}\,\mathrm{d}\Omega\,, \tag{4.24c}$$

with $\boldsymbol{O}_\mathrm{a} \in \{0\}^{8\times4}$. Consequently, $\bar{\boldsymbol{\omega}}_e$ changes to

$$\bar{\boldsymbol{\omega}}_e = \int_\Xi \boldsymbol{N}^T \boldsymbol{\omega} \det \boldsymbol{J}\, \mathrm{d}\Xi\,. \tag{4.25}$$

In conclusion, we compare the hybrid element having 8 degrees of freedom in total with the nodal element having 12 degrees of freedom. The difference in the overall degrees of freedom results from the vectorial approach to the microdistortion in the hybrid element.

5 Numerical examples

In following examples we construct analytical solutions by imposing predefined displacement and microdistortion fields and calculating the resulting right-hand side. The predefined fields are the analytical solutions to the resulting right-hand side along with the derived Dirichlet boundary conditions (for a full derivation see Appendix B). Further, in all subsequent examples the domain and the flux field $\boldsymbol{\zeta}$ lie in the $x-y$

plane and the displacement u is parallel to the z-axis. Correspondingly, for figures of u we provide a three-dimensional perspective and figures of $\boldsymbol{\zeta}$ are aerial views of the $x-y$ plane. The examples have the mechanical interpretation of a membrane antiplane deformation.

5.1 Benchmark for an imposed vanishing microdistortion

We impose the predefined fields

$$\widetilde{u}(x,y) = 4 - \frac{x^2}{8} - \frac{y^2}{8} + x\,y\,, \qquad \widetilde{\boldsymbol{\zeta}}(x,y) = 0\,. \tag{5.1}$$

In order to constrain the numerical solution to that of our proposed fields in Eq. (5.1), we set the following Dirichlet boundary conditions

$$\begin{aligned} u(x,y)\Big|_{\partial\Omega} &= \widetilde{u}(x,y)\Big|_{\partial\Omega}\,, \\ \langle \boldsymbol{\zeta}(x,y),\,\boldsymbol{\tau}\rangle\Big|_{\partial\Omega} &= \langle \widetilde{\boldsymbol{\zeta}}(x,y),\,\boldsymbol{\tau}\rangle\Big|_{\partial\Omega}\,. \end{aligned} \tag{5.2}$$

In the following example we set for simplicity

$$\mu_{\mathrm{e}} = \mu_{\mathrm{micro}} = \mu_{\mathrm{macro}} = L_{\mathrm{c}} = 1\,, \tag{5.3}$$

and extract the resulting force and moment (the right-hand side)

$$f = 1\,, \qquad \boldsymbol{\omega} = \begin{bmatrix} \frac{x}{2} - 2y \\ \frac{y}{2} - 2x \end{bmatrix}. \tag{5.4}$$

Our simulations consider the domain $\Omega = [-4,4]\times[-4,4]$ with irregular meshes under h-refinement, as shown in Fig. 7. Both element formulations converge towards the analytical solution, see Fig. 6. The microdistortion field $\boldsymbol{\zeta}$ displayed in Fig. 8 approaches zero with each refinement, satisfying the imposed field. We notice faster convergence in the hybrid element.

5.2 Benchmark for a non-vanishing imposed microdistortion

In the following step in our investigation we test our finite element formulations for a non-vanishing microdistortion field $\boldsymbol{\zeta}$, specifically a rotation field, as to determine the convergence behaviour of the nodal element with respect to the curl stiffness. We set $\Omega = [-4,4]\times[-4,4]$, $\mu_{\mathrm{e}} = \mu_{\mathrm{macro}} = \mu_{\mathrm{micro}} = L_{\mathrm{c}} = 1$ and the fields

$$\begin{aligned} \widetilde{u}(x,y) &= xy\left(\frac{y^2}{16} - \frac{x^2}{16}\right) - 1\,, \\ \widetilde{\boldsymbol{\zeta}}(x,y) &= \begin{bmatrix} -y(\frac{x^2}{8} - 2)(\frac{y^2}{8} - 2) \\ x(\frac{x^2}{8} - 2)(\frac{y^2}{8} - 2) \end{bmatrix} \end{aligned} \tag{5.5}$$

with the corresponding Dirichlet boundary conditions

$$\begin{aligned} u(x,y)\Big|_{\partial\Omega} &= \widetilde{u}(x,y)\Big|_{\partial\Omega}\,, \\ \langle \boldsymbol{\zeta}(x,y),\,\boldsymbol{\tau}\rangle\Big|_{\partial\Omega} &= \langle \widetilde{\boldsymbol{\zeta}}(x,y),\,\boldsymbol{\tau}\rangle\Big|_{\partial\Omega}\,. \end{aligned} \tag{5.6}$$

The following force and moment are extracted, for details see Appendix B,

$$f = -\frac{x\,y}{2}\left(\frac{y^2}{8} - \frac{x^2}{8}\right), \tag{5.7}$$

$$\boldsymbol{\omega} = \begin{bmatrix} -(x^2y^3)/16 + (25x^2y)/16 + (7y^3)/8 - 18y \\ (x^3y^2)/16 - (7x^3)/8 - (25xy^2)/16 + 18x \end{bmatrix}. \tag{5.8}$$

Consequently, the curl term is neither explicitly nor implicitly omitted. We compare the displacement u and the error $\|\widetilde{\boldsymbol{\zeta}} - \boldsymbol{\zeta}\|_{L^2}$ for both element formulations on an irregular mesh undergoing refinement, see Figs. 9, 10 and 11.

As shown in Fig. 10, both elements converge towards the analytical solution. However, we notice differences in the convergence rates, namely the nodal element converges faster in $\boldsymbol{\zeta}$.

5.3 Solutions in $H(\mathrm{curl})$

As $H(\mathrm{curl})$ is a larger space than $[H^1]^2$, we have the relation $[H^1]^2 \subset H(\mathrm{curl})$. Consequently, we can envision solutions belonging to $H(\mathrm{curl})$ and not $[H^1]^2$. Such solutions fulfill the continuity of tangential components along element edges of $H(\mathrm{curl})$, but not the continuity of the normal component. Elements living in $[H^1]^2$ require the continuity of both components.

In the domain $\Omega = [-4,4]\times[-4,4]$ with $\Gamma_D^u = \partial\Omega$ and $\Gamma_D^\zeta = \emptyset$ we set $\mu_{\mathrm{e}} = \mu_{\mathrm{macro}} = \mu_{\mathrm{micro}} = L_{\mathrm{c}} = 1$, the boundary conditions and external forces

$$\begin{aligned} &u(-4,y) = u(4,y) = 0\,, \qquad u(-2,y) = u(2,y) = -2\,, \\ &u(0,y) = 2\,, \qquad f = 0\,, \qquad \boldsymbol{\omega} = 0\,, \end{aligned} \tag{5.9}$$

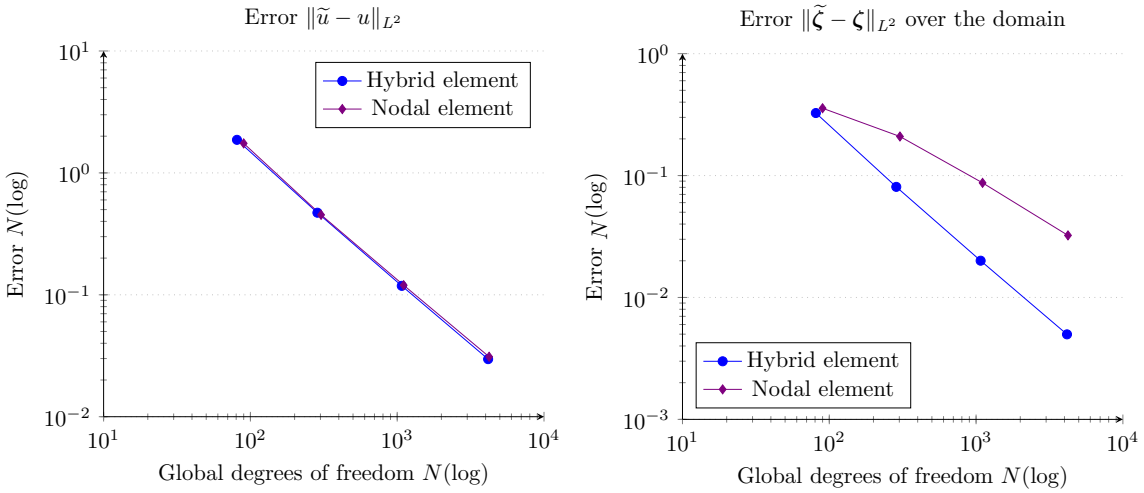

Fig. 6 Convergence behaviour of element formulations under mesh refinement

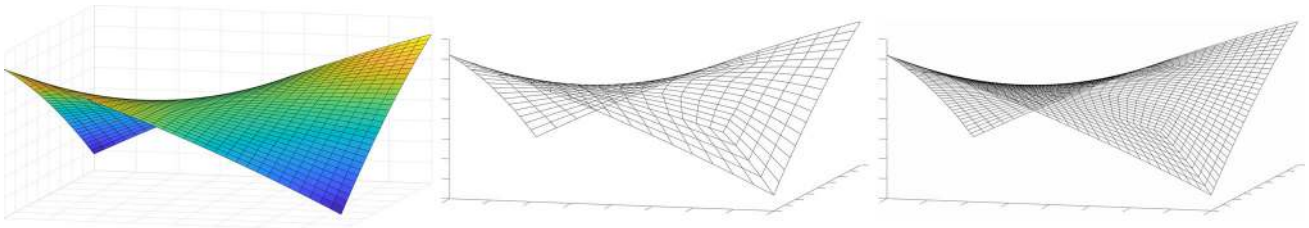

(a) Analytical solution **(b)** 336 elements **(c)** 1344 elements

Fig. 7 Displacement u of the analytical and finite element solutions

for which the analytical solution reads

$$\widetilde{u}(x,y) = \begin{cases} -4-x & \text{for} \quad -4 \le x \le -2 \\ 2+2x & \text{for} \quad -2 < x \le 0 \\ 2-2x & \text{for} \quad 0 < x \le 2 \\ x-4 & \text{for} \quad 2 < x \le 4 \end{cases},$$

$$\widetilde{\boldsymbol{\zeta}} = \frac{\nabla \widetilde{u}}{2} = \begin{cases} \begin{bmatrix} -0.5 & 0 \end{bmatrix}^T & \text{for} \quad -4 \le x \le -2 \\ \begin{bmatrix} 1 & 0 \end{bmatrix}^T & \text{for} \quad -2 < x \le 0 \\ \begin{bmatrix} -1 & 0 \end{bmatrix}^T & \text{for} \quad 0 < x \le 2 \\ \begin{bmatrix} 0.5 & 0 \end{bmatrix}^T & \text{for} \quad 2 < x \le 4 \end{cases}, \tag{5.10}$$

where $\widetilde{\boldsymbol{\zeta}}$ follows from Eqs. (2.6a) and (2.6b). Note that the boundary data of $\widetilde{\boldsymbol{\zeta}}$ jumps and is therefore not in $H^{1/2}(\Gamma_D)$. Consequently, the problem cannot be posed with $\boldsymbol{\zeta} \in [H^1(\Omega)]^2$ if we set $\Gamma_D^{\zeta} = \partial\Omega$, see Remark 3.1. For $\boldsymbol{\zeta} \in H(\text{curl}, \Omega)$ the problem could be posed as $\langle \widetilde{\boldsymbol{\zeta}}, \boldsymbol{\tau} \rangle \in L^2(\partial\Omega) \subset H^{-1/2}(\partial\Omega)$.

We test both elements on an irregular mesh undergoing refinement Fig. 12. We note the hybrid element finds the exact solution immediately with a coarse mesh, whereas the nodal element requires a much higher level of refinement in order to deliver a viable approximation. The nodal element localizes the error due to the discontinuity further with each refinement as seen in Fig. 13. The convergence graph in Fig. 14 depicts the slow sub-optimal convergence of the nodal element, compare Eq. (3.28). Note, the error in the hybrid element for the same meshes is always at a factor 10^{-15} for both u and $\boldsymbol{\zeta}$. Due to the higher continuity conditions of the nodal element, it could never find the analytical solution, but would converge further towards it with each refinement.

We present a second example allowing us to compare the convergence rates for both formulations. Let $\Omega = [0,1] \times [0,1]$, $\mu_e = \mu_{\text{macro}} = \mu_{\text{micro}} = L_c = 1$, and $\Gamma_D^u = \Gamma_D^{\zeta} = \partial\Omega$. For the given exact solution $\{\widetilde{u}, \widetilde{\boldsymbol{\zeta}}\} \in H_0^1(\Omega) \times H_0(\text{curl}\,\Omega)$

$$\widetilde{u}(x,y) = \exp(1-x)y(1-y) \begin{cases} x & \text{for } x \le 0.5 \\ 1-x & \text{for } x > 0.5 \end{cases},$$
$$\widetilde{\boldsymbol{\zeta}} = \nabla \widetilde{u}\,, \tag{5.11}$$

the corresponding boundary conditions and external forces result in

$$u(x,y)\Big|_{\partial\Omega} = 0, \quad \langle \boldsymbol{\zeta}, \boldsymbol{\tau} \rangle\Big|_{\partial\Omega} = 0, \qquad f = 0, \quad \boldsymbol{\omega} = 2\widetilde{\boldsymbol{\zeta}}\,. \tag{5.12}$$

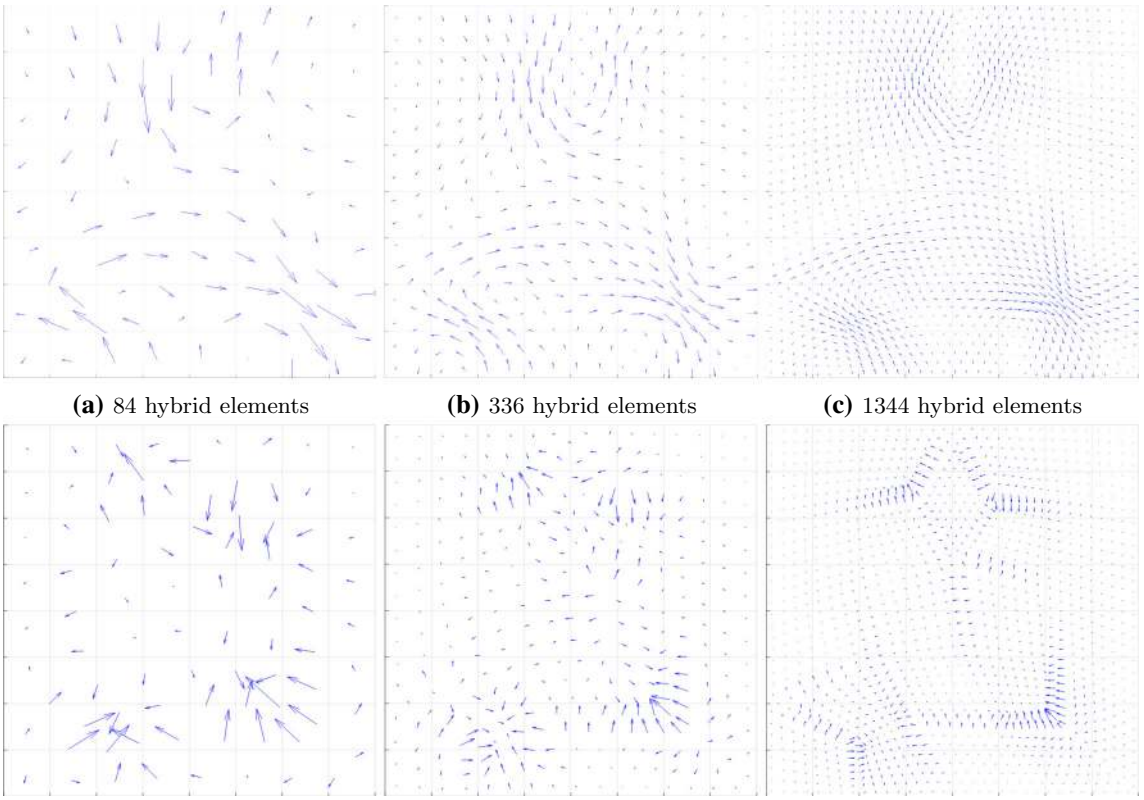

(a) 84 hybrid elements **(b)** 336 hybrid elements **(c)** 1344 hybrid elements

(d) 84 nodal elements **(e)** 336 nodal elements **(f)** 1344 nodal elements

Fig. 8 Decay of the microdistortion ζ according to Eq. (5.1) on irregular meshes undergoing refinement. The intensity of the microdistortion approaches zero with each refinement. This is seen here in a decrease of the flux vectors

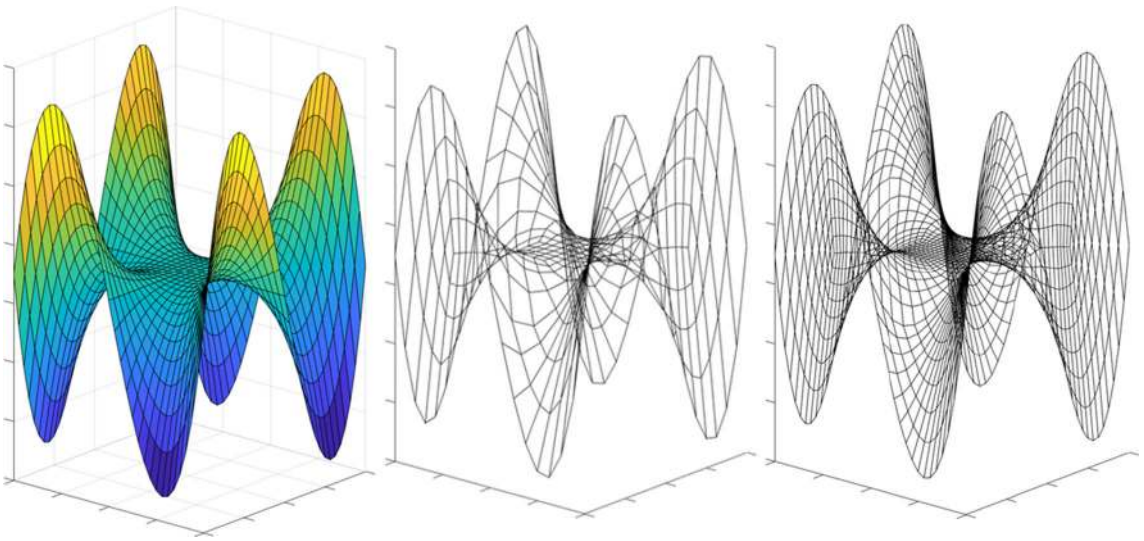

(a) Analytical solution **(b)** 256 elements **(c)** 1024 elements

Fig. 9 Displacement u of the analytical and finite element solutions

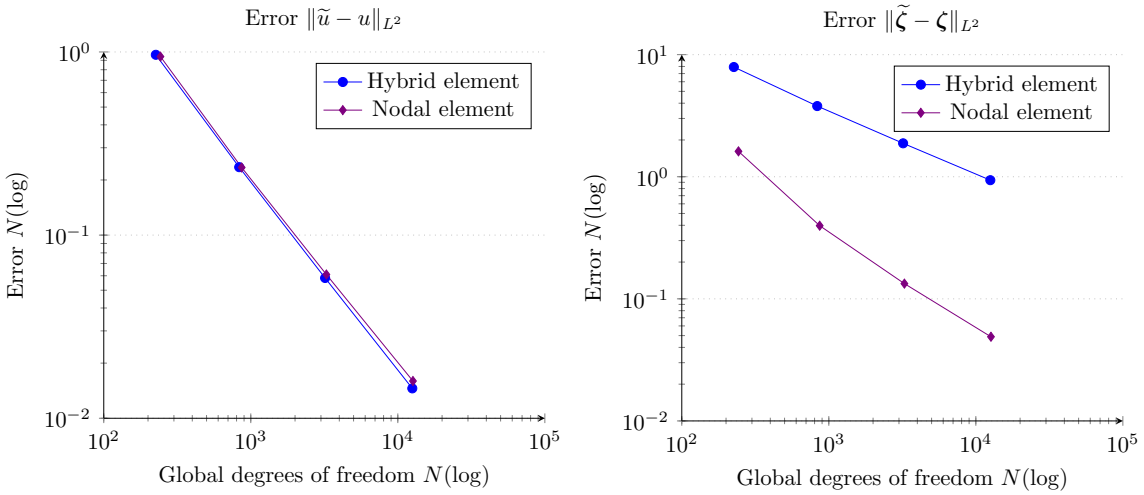

Fig. 10 Convergence behaviour of element formulations under mesh refinement

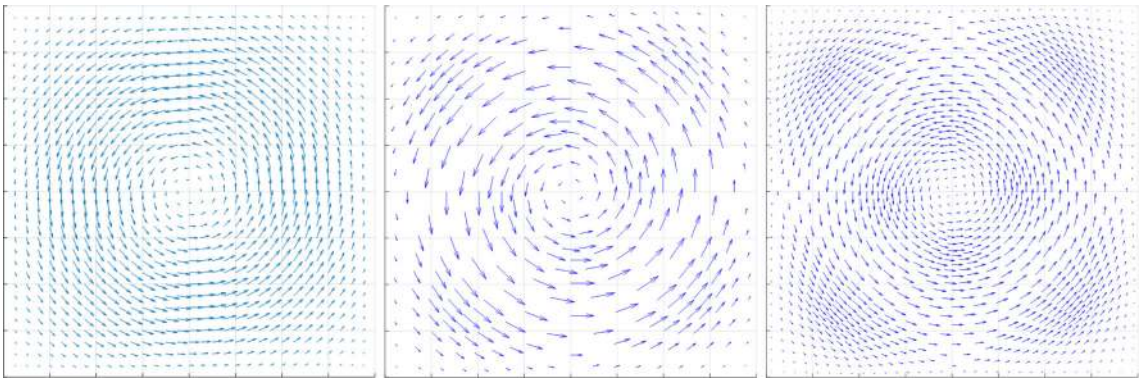

(a) Analytical flux solution **(b)** 256 elements **(c)** 1024 elements

Fig. 11 Microdistortion ζ of the analytical and finite element solutions on unstructured grids according to Eq. (5.5)

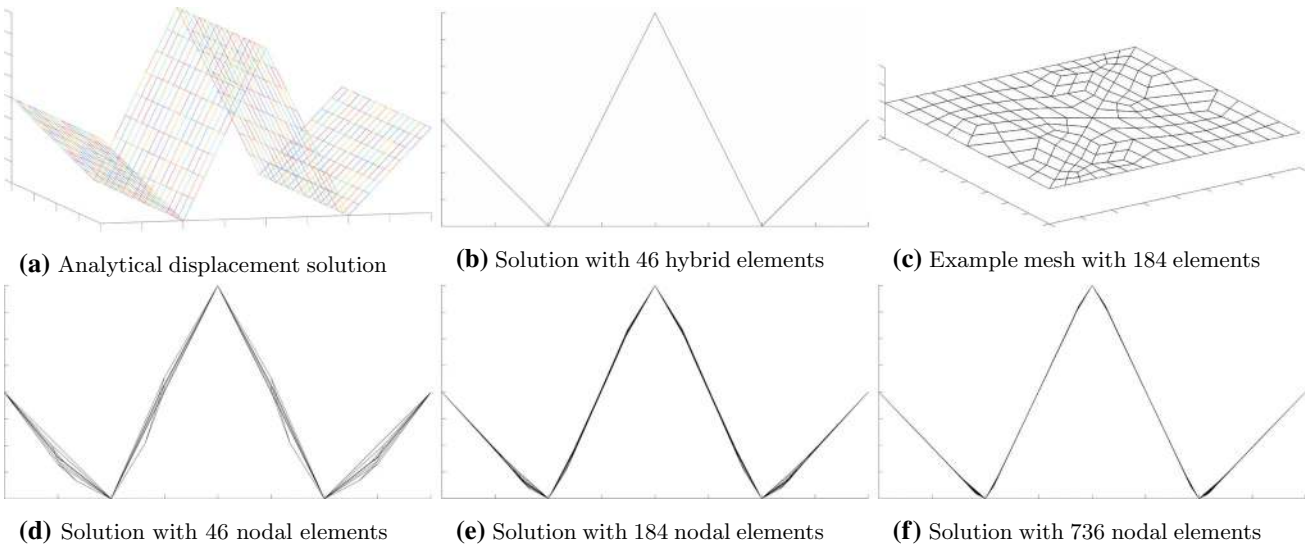

(a) Analytical displacement solution **(b)** Solution with 46 hybrid elements **(c)** Example mesh with 184 elements

(d) Solution with 46 nodal elements **(e)** Solution with 184 nodal elements **(f)** Solution with 736 nodal elements

Fig. 12 Analytical solution and finite element front view ($x - z$ plane) for solutions of Eq. (5.10)

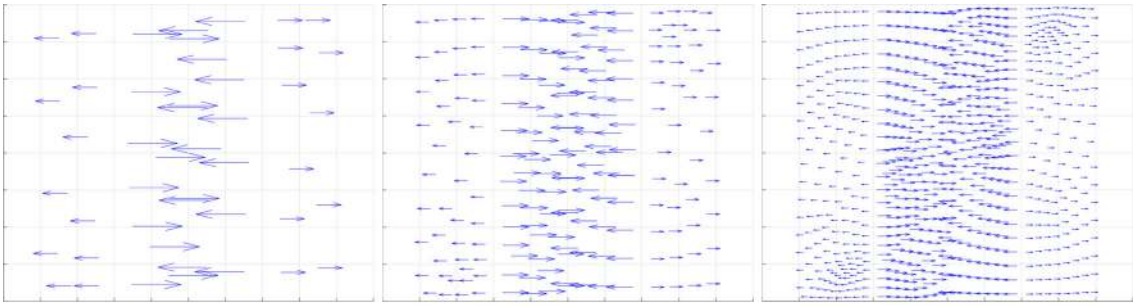

(a) Microdistortion with 46 hybrid elements **(b)** Microdistortion with 184 hybrid elements **(c)** Microdistortion with 736 hybrid elements

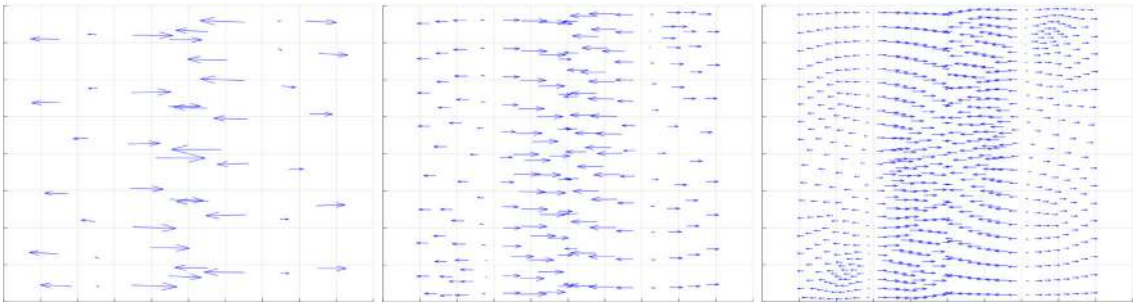

(d) Microdistortion with 46 nodal elements **(e)** Microdistortion with 184 nodal elements **(f)** Microdistortion with 736 nodal elements

Fig. 13 Finite element solutions of the microdistortion for Eq. (5.10) for both formulations

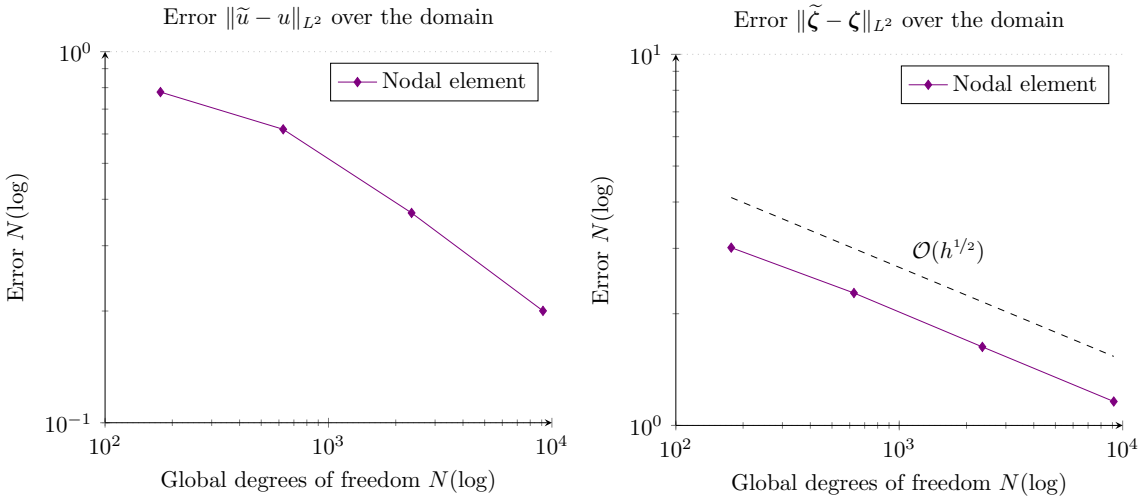

Fig. 14 Convergence behaviour of element formulations under mesh refinement

Here, the boundary conditions are compatible with $\boldsymbol{\zeta} \in [H^1(\Omega)]^2$, but the exact solution is only in $H(\mathrm{curl}, \Omega)$, not in $[H^1(\Omega)]^2$. We use structured quadrilateral meshes (see Fig. 16) resolving the interface at $x = 0.5$, where the normal component of the exact solution of $\boldsymbol{\zeta}$ jumps, with linear, quadratic and cubic polynomials for the nodal elements. We observe that higher polynomial degrees do not increase the convergence rate and only sub-optimal root-convergence is achieved (see Fig. 15). For linear and quadratic ansatz functions in the primal $H(\mathrm{curl})$ method we observe optimal convergence rates.

5.4 Convergence for $L_c \to 0$

As mentioned in Section 3, the characteristic length L_c represents an important term in the relaxed micromorphic theory. This scalar governs the relation of the relaxed micromorphic continuum to the standard Cauchy continuum. In the previous examples we have been able to generate stable results for the case $L_c = 1$. In this example we consider the limit $L_c \to 0$, which can be interpreted as a highly homogenous material. In the $L_c = 0$ setting, the relaxed

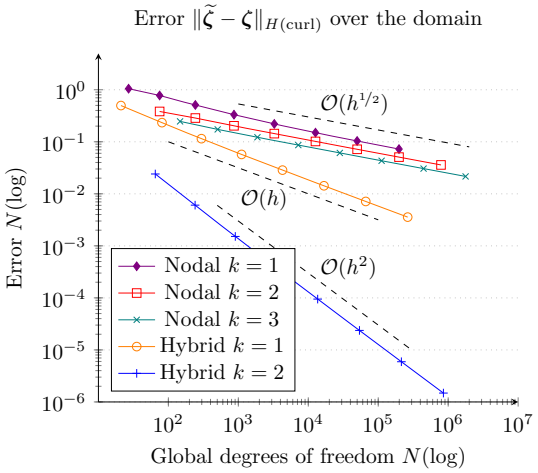

Fig. 15 Convergence rates of the microdistortion on both element formulations across multiple polynomial degrees undergoing mesh refinement

micromorphic continuum retrieves the results of the classical Cauchy continuum, no external moments $\boldsymbol{\omega}$ occur and the microdistortion $\boldsymbol{\zeta}$ lives in $[L^2(\Omega)]^2$. This results in the emergence of a single Poisson equation for u (see Remark 3.2), being an analogue of the standard membrane partial differential equation. We define the domain $\Omega = [-5,\ 5] \times [-5,\ 5]$ with $\mu_\mathrm{e},\ \mu_\mathrm{micro} = 1,\ L_\mathrm{c} = 0$ and the imposed displacement

$$\widetilde{u}(x,\, y) = 2 - \sin(x)^2 + \cos(x)^2 - \sin(y)^2 + \cos(y)^2\,. \tag{5.13}$$

We use $\widetilde{u}$ to recover the analytical solution for $\widetilde{\boldsymbol{\zeta}}$

$$\widetilde{\boldsymbol{\zeta}} = \frac{\mu_\mathrm{e}}{\mu_\mathrm{micro} + \mu_\mathrm{e}} \nabla \widetilde{u} = \begin{bmatrix} -2\cos(x)\sin(x) \\ -2\cos(y)\sin(y) \end{bmatrix}, \tag{5.14}$$

and the resulting right-hand side

$$f = 4\left(\cos(x)^2 + \cos(y)^2 - \sin(x)^2 - \sin(y)^2\right). \tag{5.15}$$

Note, since we require $\boldsymbol{\zeta} \in [L^2(\Omega)]^2$, no boundary conditions can be prescribed for $\boldsymbol{\zeta}$. The microdistortion field $\boldsymbol{\zeta}$ can always be approximated using either $H(\mathrm{curl})$ or $[H^1]^2$ elements. However, the direct use of discontinuous $[L^2]^2$ elements for $\boldsymbol{\zeta}$ requires less computation and can also capture gradient fields. With Theorem 3.3 we have for $\boldsymbol{\omega} = 0$ the regularity result that $\boldsymbol{\zeta}$ is in fact a gradient field and thus $\boldsymbol{\zeta} \in H(\mathrm{curl}, \Omega)$, which confirms to use Nédélec elements without risk of sub-optimal convergence rates, compare Sect. 5.3. The finite element solution converges towards the analytical solution as expected with optimal rate, see Figs. 17 and 18.

5.5 Robustness in L_c

The upper limit of the characteristic length L_c is defined to be infinity. In this example we prove the robustness of our computations for $L_\mathrm{c} \to \infty$. The analytical solution on $\Omega = [-4, 4] \times [-4, 4]$ with homogeneous Dirichlet data on $\partial\Omega$ and $\mu_\mathrm{e} = \mu_\mathrm{macro} = \mu_\mathrm{micro} = 1$ is given by

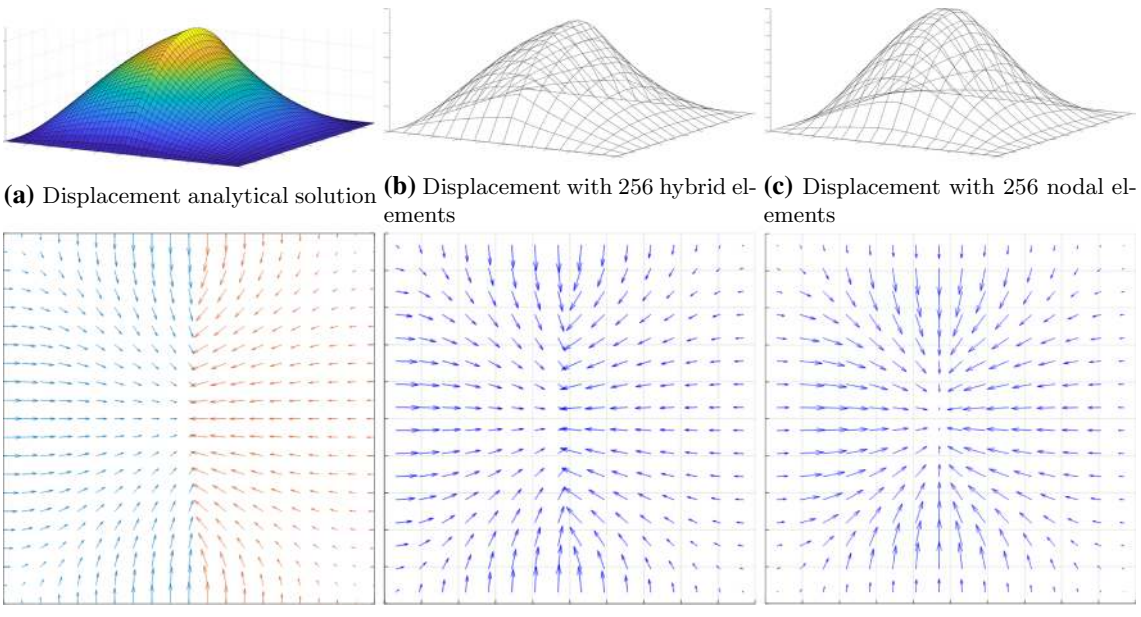

(a) Displacement analytical solution **(b)** Displacement with 256 hybrid elements **(c)** Displacement with 256 nodal elements

(d) Microdistortion analytical solution **(e)** Microdistortion with 256 hybrid elements **(f)** Microdistortion with 256 nodal elements

Fig. 16 Analytical and finite element solutions of the displacement and microdistortion fields according to Eq. (5.11)

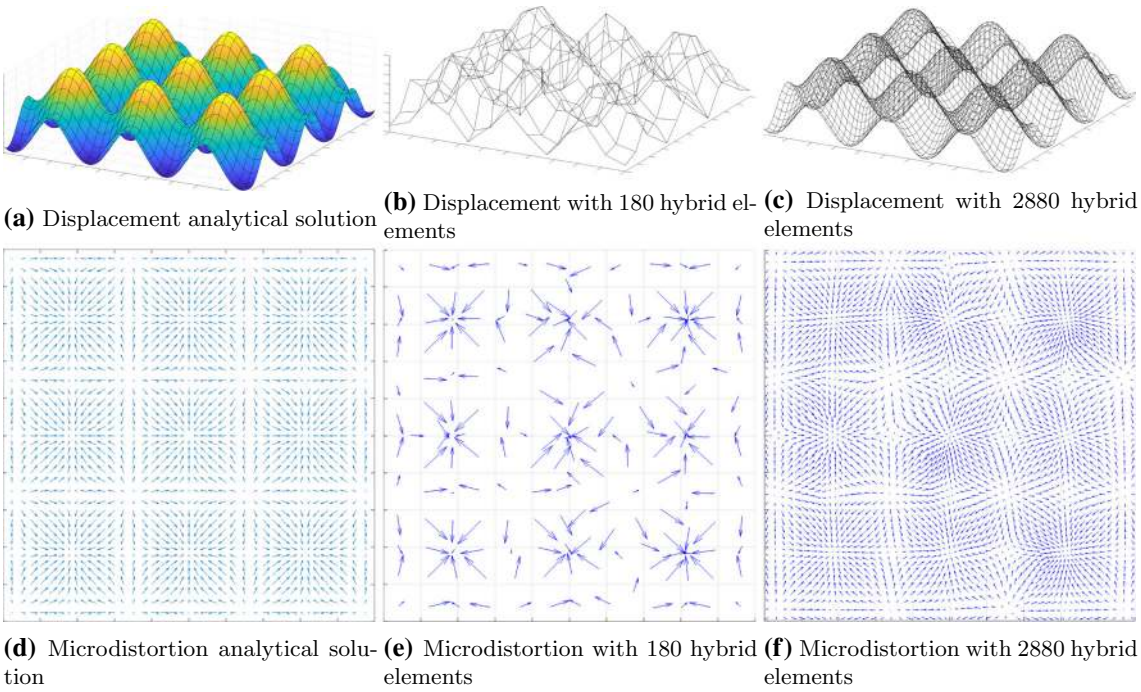

(a) Displacement analytical solution **(b)** Displacement with 180 hybrid elements **(c)** Displacement with 2880 hybrid elements

(d) Microdistortion analytical solution **(e)** Microdistortion with 180 hybrid elements **(f)** Microdistortion with 2880 hybrid elements

Fig. 17 Analytical solutions and finite element solutions on unstructured grids of the displacement and microdistortion fields according to Eqs. (5.13) and (5.14)

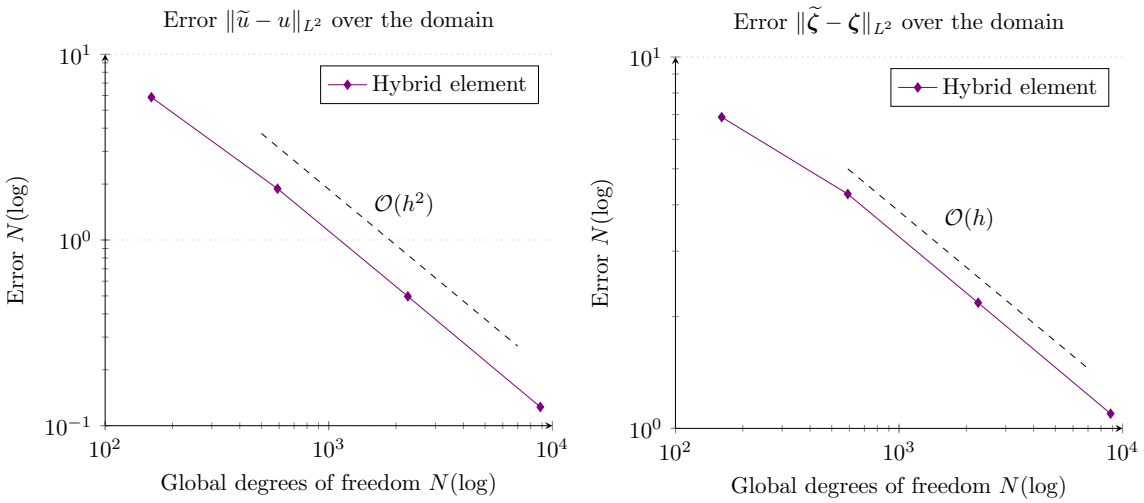

Fig. 18 Convergence behaviour of the hybrid element formulation under mesh refinement for the case $L_c = 0$

$$\widetilde{u}(x, y) = \cos\left(\frac{\pi x}{8}\right)(y^2 - 16)\exp\left(\frac{x + y}{100}\right), \tag{5.16a}$$

$$\widetilde{\boldsymbol{\zeta}}(x, y) = 2\begin{bmatrix} x(y^2 - 16) \\ y(x^2 - 16) \end{bmatrix} + \frac{1}{L_c^2}\left(\frac{x^2}{8} - 2\right)\left(\frac{y^2}{8} - 2\right)\begin{bmatrix} -y \\ x \end{bmatrix}, \tag{5.16b}$$

from which we can extract the resulting force fields according to Eqs. (2.6a) and (2.6b). We test for convergence using linear elements.

As expected from the theory, we observe uniform convergence up to the point where rounding errors occur in the primal method for very large L_c terms. The convergences of the mixed formulation remains stable for all values of L_c as it is not affected by rounding errors, cf. Fig. 19. Using lowest order linear nodal elements for $\boldsymbol{\zeta}$ leads to non-robust behaviour in L_c in terms of immense locking. Considering quadratic Lagrange elements overcomes this locking phenomena, however, at the cost of more dofs.

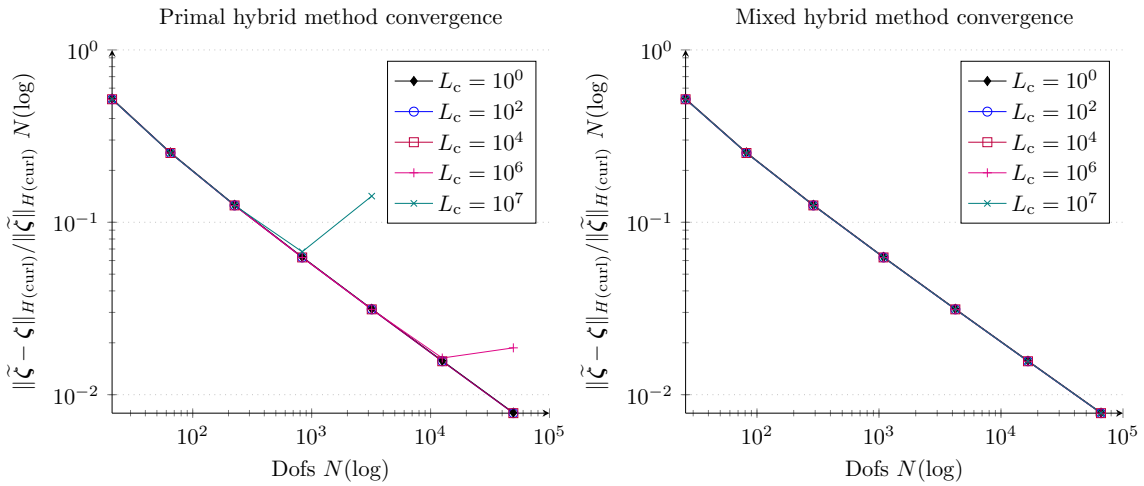

Fig. 19 Convergence behaviour for fixed L_c on 1×1, 2×2, 4×4, 8×8, 16×16, 32×32, and 64×64 structured quadrilateral grids for the primal and mixed hybrid methods

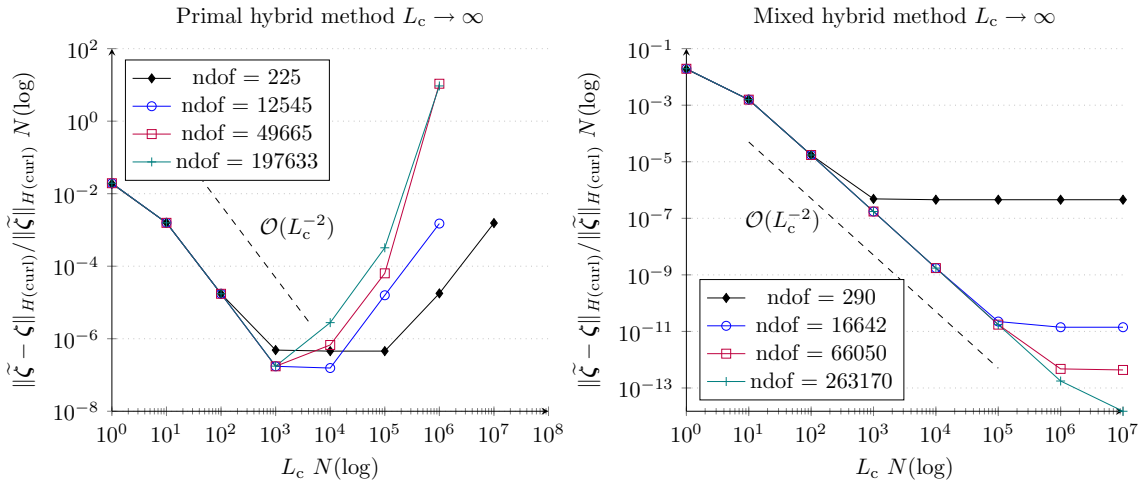

Fig. 20 Convergence behaviour for $L_c \to \infty$ for fixed 4×4, 16×16, 32×32, 64×64 and 128×128 grids

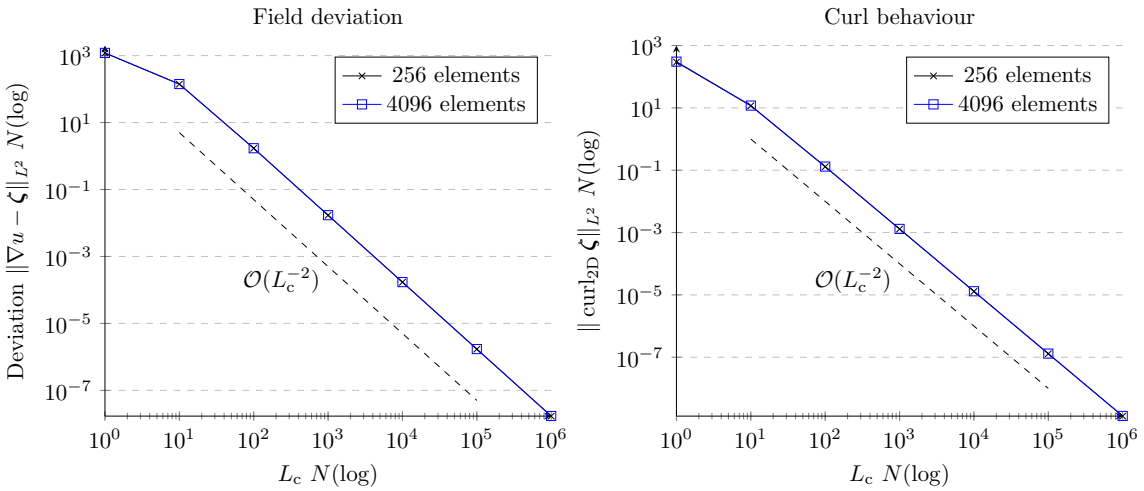

Fig. 21 Convergence behaviour of the difference $\nabla u - \zeta$ and $\operatorname{curl}_{2D} \zeta$ for $L_c \to \infty$ with primal hybrid method

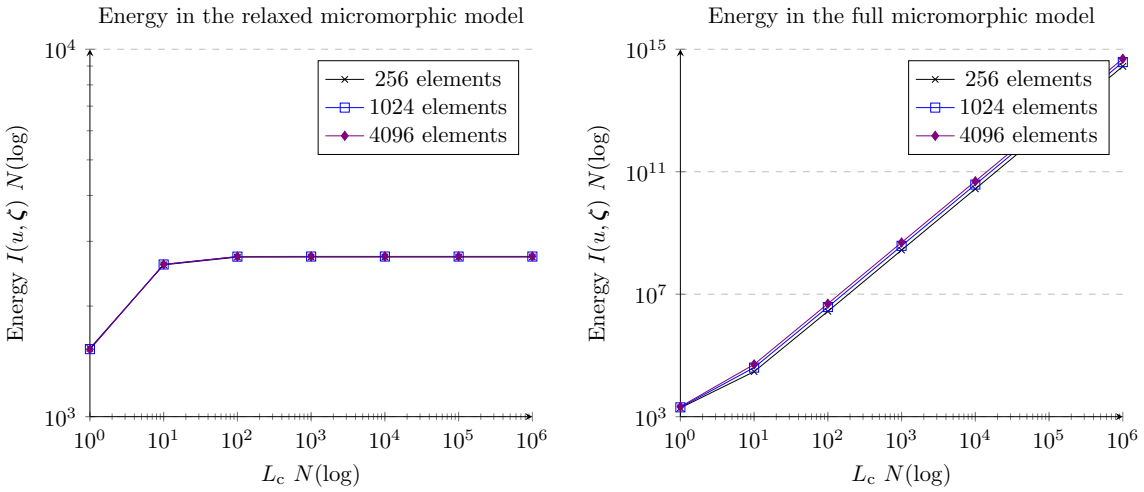

Fig. 22 Energy convergence in the relaxed and full micromorphic models according to Eq. (5.18)

To test the convergence depending on L_c, Eq. (3.18), for the case $L_c \to \infty$ we use quadratic elements - i.e., quadratic H^1 and Nédélec elements, and linear L^2 elements for m in the mixed formulation - in NGSolve and four different structured grids. The same domain as in the previous example is considered and for the limit solution Eq. (5.16) is used, with $L_c \to \infty$ in Eq. (5.16b). Again, the primal methods suffers for large values of L_c from rounding errors, whereas for the mixed method we observe the expected quadratic convergence rate up to the discretization error, compare Eq. (3.32) and Fig. 20.

5.6 Convergence for $L_c \to \infty$

We prove the theoretical result of Theorem 3.5, with the same domain, boundary conditions, and material constants as in the previous example, by setting the external force and moments

$$f = 0\,, \quad r = (16 - x^2)(16 - y^2)(xy - y^2)\,,$$
$$\Psi = x^3y^2 - xy^2(1 - x) - \frac{256}{9}\,, \quad \boldsymbol{\omega} = \nabla r + \mathrm{D}^{\mathrm{curl}}(\Psi)\,, \tag{5.17}$$

and testing for convergence $\|\nabla u - \boldsymbol{\zeta}\|_{H(\mathrm{curl})} = \mathcal{O}(L_c^{-2})$ for $L_c \to \infty$ using NGSolve with linear base functions.

The results are computed using the primal method. By staying within the rounding precision bounds retrieved from our investigation of the robustness in L_c, we are able to find results converging quadratically to the previously derived expectations, see Fig. 21.

5.7 The consistent coupling condition

We conclude our investigation by considering the consistent coupling condition on both the full and relaxed micromorphic continuum models using NGSolve with the primal method. We set the domain $\Omega = [-4, 4] \times [-4, 4]$ with the material parameters $\mu_e,\ \mu_{\mathrm{micro}}, \mu_{\mathrm{macro}} = 1$, the boundary conditions

$$u(x, y)\Big|_{\partial\Omega} = y^2 - x^2,$$
$$\langle \boldsymbol{\zeta},\ \boldsymbol{\tau}\rangle\Big|_{\partial\Omega} = \langle \nabla u,\ \boldsymbol{\tau}\rangle\Big|_{\partial\Omega} = \Big\langle \begin{bmatrix}-2x & 2y\end{bmatrix}^T,\ \boldsymbol{\tau}\Big\rangle\Big|_{\partial\Omega}, \tag{5.18}$$

and the external forces

$$f = 0\,, \qquad \boldsymbol{\omega} = \begin{bmatrix}-y & x\end{bmatrix}^T\,, \tag{5.19}$$

and test for convergence in both micromorphic formulations with increasing characteristic lengths L_c.

As observed in Fig. 22, the relaxed micromorphic continuum converges towards a finite energy, whereas the non-trivial boundary conditions on the full micromorphic continuum lead to boundary-layers and consequently, ever-increasing energy for $L_c \to \infty$. The result is consistent with the problematic mentioned in Remark 3.5.

6 Conclusions and outlook

The relaxed micromorphic continuum theory introduces the Curl operator in the formulation of the free energy functional. As a result, the solution of the weak form lies in the combined space $H^1 \times H(\mathrm{curl})$. The Lax–Milgram theorem confirms this result by assuring existence and uniqueness for the combined space. Our benchmarks with a completely nodal finite element show its capacity to approximate solutions in the combined space. However, the tests also show its inability to find the exact solution for discontinuous microdistortion fields and the corresponding sub-optimal convergence. A

comparison between the linear nodal and hybrid element formulations also reveals the difference in the arising elemental stiffness matrices, namely $\boldsymbol{K}_{\text{nodal}} \in \mathbb{R}^{12\times 12}$ and $\boldsymbol{K}_{\text{hybrid}} \in \mathbb{R}^{8\times 8}$, resulting in slower computation times for the nodal element. In contrast, the hybrid element yields stable approximations and convergence rates for all tested scenarios, being capable of finding the exact solution also for discontinuous microdistortion fields. The relaxed micromorphic theory aims to capture the mechanical behaviour of metamaterials, highly homogeneous materials and the entire spectrum in between. To that end, the characteristic length L_c takes the role of a weighting parameter, determining the influence of the energy from the dislocation density (the energy depending on the curl operator). The range of the characteristic length L_c is an open topic of research into metamaterials. However, from a theoretical point of view, it may vary between zero and infinity. Our tests reveal the arising instability of convergence where increasingly large L_c parameters are concerned and emergence of locking effects if linear nodal elements are chosen to approximate the microdistortion. For the case of the hybrid element, lost precision can be recovered via the formulation of the corresponding mixed problem. Locking effects in the nodal version of the microdistortion can be alleviated via higher order polynomials at the cost of increased dofs. In addition, also in $L_c = 0$ setting, where the external moment $\boldsymbol{\omega}$ vanishes, we recognize the optimality of using $H(\text{curl})$-elements for the computation of the microdistortion, seeing as it is in fact the natural space for the microdistortion in this setting. Lastly, we recognize the advantage of the relaxed micromorphic continuum with regard to its ability to generate finite energies as $L_c \to \infty$ for arbitrary boundary conditions.

These findings build the basis for the extension of the formulation to the fully three-dimensional or a statically condensed two-dimensional version of the full relaxed micromorphic continuum.

Acknowledgements The support by the Austrian Science Fund (FWF) project W 1245 is gratefully acknowledged. P. Neff acknowledges support in the framework of the DFG Priority Programme 2256 Variational Methods for Predicting Complex Phenomena in Engineering Structures and Materials Neff 902/10-1, No: 440935806.
The authors are very grateful to the referees for their comments.

Funding Open Access funding enabled and organized by Projekt DEAL.

A Derivation of the strong form

In order to find the strong form of the Euler-Lagrange equations to Problem 3.4 we start with the most general setting $\Gamma^u_D \cap \Gamma^u_N = \emptyset$, $\overline{\Gamma^u_D} \cup \overline{\Gamma^u_N} = \partial\Omega$ and $\Gamma^\zeta_D \cap \Gamma^\zeta_N = \emptyset$, $\overline{\Gamma^\zeta_D} \cup \overline{\Gamma^\zeta_N} = \partial\Omega$. The Dirichlet and Neumann boundary parts of u and $\boldsymbol{\zeta}$ and assume that $|\Gamma^u_D| > 0$ (for Lax–Milgram solvability). We assume smooth fields such that we can integrate by parts. Using the Green identity

$$\begin{aligned}&\int_\Omega \operatorname{div} q\,\mathbf{v}\,\mathrm{d}X = \oint_{\partial\Omega} \langle q\,\boldsymbol{\nu},\,\mathbf{v}\rangle\,\mathrm{d}s - \int_\Omega \langle \nabla q,\,\mathbf{v}\rangle\,\mathrm{d}X\,,\\ &\mathbf{v}\in C^1(\Omega,\mathbb{R}^2)\,,\quad q\in C^1(\Omega,\mathbb{R})\,,\end{aligned}\tag{A.1}$$

where $\boldsymbol{\nu}$ is the normal vector on the boundary, and splitting the boundary terms of the first weak form Eq. (2.5a), we find

$$\begin{aligned}&\int_\Omega 2\mu_e\langle(\nabla u-\boldsymbol{\zeta}),\,\nabla\delta u\rangle - \langle\delta u,\,f\rangle\,\mathrm{d}X\\ &=\int_{\Gamma^u_D}\delta u\langle(\nabla u-\boldsymbol{\zeta}),\,\boldsymbol{\nu}\rangle\,\mathrm{d}s+\int_{\Gamma^u_N}\delta u\langle(\nabla u-\boldsymbol{\zeta}),\,\boldsymbol{\nu}\rangle\,\mathrm{d}s\\ &\quad-\int_\Omega\langle\operatorname{div}(\nabla u-\boldsymbol{\zeta})-f,\,\delta u\rangle\,\mathrm{d}X=0\\ &\quad\text{for all }\delta u\in C^1(\Omega,\mathbb{R})\,.\end{aligned}\tag{A.2}$$

As the Dirichlet data is directly incorporated into the space we have $\delta u = 0$ on Γ^u_D and thus, for given Dirichlet data $\widetilde{u}$, we obtain the strong form

$$\begin{aligned}-2\mu_e\operatorname{div}(\nabla u-\boldsymbol{\zeta}) &= f && \text{in }\Omega\,,\\ u &= \widetilde{u} && \text{on }\Gamma^u_D\,,\\ \langle\nabla u,\,\boldsymbol{\nu}\rangle &= \langle\boldsymbol{\zeta},\,\boldsymbol{\nu}\rangle && \text{on }\Gamma^u_N\,.\end{aligned}\tag{A.3}$$

For the second weak form Eq. (2.5b) we employ another Green identity

$$\begin{aligned}&\int_\Omega \lambda\,\operatorname{curl}_{2D}\mathbf{q}\,\mathrm{d}X = \oint_{\partial\Omega}\langle\lambda\,\mathbf{q},\,\boldsymbol{\tau}\rangle\,\mathrm{d}s+\int_\Omega\langle\mathrm{D}^{\mathrm{curl}}\lambda,\,\mathbf{q}\rangle\,\mathrm{d}X\,,\\ &\lambda\in C^1(\Omega,\mathbb{R})\,,\quad\mathbf{q}\in C^1(\Omega,\mathbb{R}^2)\,,\end{aligned}\tag{A.4}$$

and split the boundary, obtaining for all $\delta\boldsymbol{\zeta} \in C^1(\Omega, \mathbb{R}^2)$

$$\begin{aligned}
&\int_\Omega 2\mu_\mathrm{e}\,\langle(\nabla u - \boldsymbol{\zeta}),\,(-\delta\boldsymbol{\zeta})\rangle + 2\mu_\mathrm{micro}\,\langle\boldsymbol{\zeta},\,\delta\boldsymbol{\zeta}\rangle \\
&\quad + \mu_\mathrm{macro}\,L_\mathrm{c}^2\,\langle\mathrm{curl}_\mathrm{2D}\,\boldsymbol{\zeta},\,\mathrm{curl}_\mathrm{2D}\,\delta\boldsymbol{\zeta}\rangle - \langle\delta\boldsymbol{\zeta},\,\boldsymbol{\omega}\rangle\,\mathrm{d}X \\
&= \int_\Omega 2\mu_\mathrm{e}\,\langle(\nabla u - \boldsymbol{\zeta}),\,(-\delta\boldsymbol{\zeta})\rangle + 2\mu_\mathrm{micro}\,\langle\boldsymbol{\zeta},\,\delta\boldsymbol{\zeta}\rangle \\
&\quad + \mu_\mathrm{macro}\,L_\mathrm{c}^2\langle\mathrm{D}^\mathrm{curl}(\mathrm{curl}_\mathrm{2D}\,\boldsymbol{\zeta}),\,\delta\boldsymbol{\zeta}\rangle - \langle\delta\boldsymbol{\zeta},\,\boldsymbol{\omega}\rangle\,\mathrm{d}X \\
&+ \int_{\Gamma_D^\zeta} \mu_\mathrm{macro}\,L_\mathrm{c}^2\,\mathrm{curl}_\mathrm{2D}(\boldsymbol{\zeta})\langle\delta\boldsymbol{\zeta},\,\boldsymbol{\tau}\rangle\,\mathrm{d}s \\
&\quad + \int_{\Gamma_N^\zeta} \mu_\mathrm{macro}\,L_\mathrm{c}^2\,\mathrm{curl}_\mathrm{2D}(\boldsymbol{\zeta})\langle\delta\boldsymbol{\zeta},\,\boldsymbol{\tau}\rangle\,\mathrm{d}s = 0\,. \qquad \text{(A.5)}
\end{aligned}$$

Again, the Dirichlet data is incorporated into the space, such that the following strong formulation arises

$$\begin{aligned}
&-2\mu_\mathrm{e}(\nabla u - \boldsymbol{\zeta}) + 2\mu_\mathrm{micro}\boldsymbol{\zeta} + \mu_\mathrm{macro}L_\mathrm{c}^2\,\mathrm{D}^\mathrm{curl}(\mathrm{curl}_\mathrm{2D}\,\boldsymbol{\zeta}) \\
&\quad = \boldsymbol{\omega} \quad \text{in } \Omega\,, \\
&\mathrm{curl}_\mathrm{2D}\,\boldsymbol{\zeta} = 0 \quad \text{on } \Gamma_N^\zeta\,, \\
&\langle\boldsymbol{\zeta},\,\boldsymbol{\tau}\rangle = \langle\widetilde{\boldsymbol{\zeta}},\,\boldsymbol{\tau}\rangle \quad \text{on } \Gamma_D^\zeta\,. \qquad \text{(A.6)}
\end{aligned}$$

The complete boundary value problem is given by Eqs. (A.3) and (A.6).

B Constructing analytical solutions

The predefined fields are given by $\widetilde{u}$ and $\widetilde{\boldsymbol{\zeta}}$. We redefine the variables of the strong form $u^* = u - \widetilde{u}$ and $\boldsymbol{\zeta}^* = \boldsymbol{\zeta} - \widetilde{\boldsymbol{\zeta}}$ and insert them into the partial differential equation

$$\begin{aligned}
&-2\mu_\mathrm{e}\,\mathrm{div}(\nabla(u - \widetilde{u}) - (\boldsymbol{\zeta} - \widetilde{\boldsymbol{\zeta}})) = 0\,, \qquad \text{(B.1a)} \\
&-2\mu_\mathrm{e}(\nabla(u - \widetilde{u}) - (\boldsymbol{\zeta} - \widetilde{\boldsymbol{\zeta}})) + 2\mu_\mathrm{micro}(\boldsymbol{\zeta} - \widetilde{\boldsymbol{\zeta}}) \\
&\quad + \mu_\mathrm{macro}L_\mathrm{c}^2\,\mathrm{D}^\mathrm{curl}\,\mathrm{curl}_\mathrm{2D}(\boldsymbol{\zeta} - \widetilde{\boldsymbol{\zeta}}) = 0\,, \qquad \text{(B.1b)}
\end{aligned}$$

yielding compositions of additive terms. Therefore, we can rearrange the equations

$$\begin{aligned}
&2\mu_\mathrm{e}\,\mathrm{div}(\nabla u - \boldsymbol{\zeta}) = 2\mu_\mathrm{e}\,\mathrm{div}(\nabla\widetilde{u} - \widetilde{\boldsymbol{\zeta}})\,, \\
&-2\mu_\mathrm{e}(\nabla u - \boldsymbol{\zeta}) + 2\mu_\mathrm{micro}\boldsymbol{\zeta} + \mu_\mathrm{macro}L_\mathrm{c}^2\,\mathrm{D}^\mathrm{curl}(\mathrm{curl}_\mathrm{2D}\,\boldsymbol{\zeta}) \\
&\quad = -2\mu_\mathrm{e}(\nabla\widetilde{u} - \widetilde{\boldsymbol{\zeta}}) + 2\mu_\mathrm{micro}\widetilde{\boldsymbol{\zeta}} \\
&\qquad + \mu_\mathrm{macro}L_\mathrm{c}^2\,\mathrm{D}^\mathrm{curl}(\mathrm{curl}_\mathrm{2D}\,\widetilde{\boldsymbol{\zeta}})\,. \qquad \text{(B.2a)}
\end{aligned}$$

It is clear that the solutions of the PDE must be $u = \widetilde{u}$ and $\boldsymbol{\zeta} = \widetilde{\boldsymbol{\zeta}}$. Since both $\widetilde{u}$ and $\widetilde{\boldsymbol{\zeta}}$ are known a priori, their insertion in the PDE can be calculated. We define the calculated fields

$$\begin{aligned}
f &:= -2\mu_\mathrm{e}\,\mathrm{div}(\nabla\widetilde{u} - \widetilde{\boldsymbol{\zeta}})\,, \\
\boldsymbol{\omega} &:= -2\mu_\mathrm{e}(\nabla\widetilde{u} - \widetilde{\boldsymbol{\zeta}}) + 2\mu_\mathrm{micro}\widetilde{\boldsymbol{\zeta}} \\
&\quad + \mu_\mathrm{macro}L_\mathrm{c}^2\,\mathrm{D}^\mathrm{curl}(\mathrm{curl}_\mathrm{2D}\,\widetilde{\boldsymbol{\zeta}})\,. \qquad \text{(B.3)}
\end{aligned}$$

The strong forms with the newly found right-hand sides are multiplied with the corresponding test functions

$$\begin{aligned}
&\int_\Omega 2\mu_\mathrm{e}\langle\mathrm{div}(\nabla u - \boldsymbol{\zeta}),\,\delta u\rangle\,\mathrm{d}X = -\int_\Omega \langle f,\,\delta u\rangle\,\mathrm{d}X\,, \qquad \text{(B.4a)} \\
&\int_\Omega -2\mu_\mathrm{e}\langle(\nabla u - \boldsymbol{\zeta}),\,\delta\boldsymbol{\zeta}\rangle + 2\mu_\mathrm{micro}\langle\boldsymbol{\zeta},\,\delta\boldsymbol{\zeta}\rangle \\
&\quad + \mu_\mathrm{macro}L_\mathrm{c}^2\langle\mathrm{D}^\mathrm{curl}(\mathrm{curl}_\mathrm{2D}\,\boldsymbol{\zeta}),\,\delta\boldsymbol{\zeta}\rangle\,\mathrm{d}X = \int_\Omega \langle\boldsymbol{\omega},\,\delta\boldsymbol{\zeta}\rangle\,\mathrm{d}X\,. \qquad \text{(B.4b)}
\end{aligned}$$

Employing Greens' identities Eqs. (A.1 and (A.4) we find

$$\begin{aligned}
&\oint_{\partial\Omega} 2\mu_\mathrm{e}\,\delta u\langle(\nabla u - \boldsymbol{\zeta}),\,\boldsymbol{\nu}\rangle\,\mathrm{d}s - \int_\Omega 2\mu_\mathrm{e}\langle(\nabla u - \boldsymbol{\zeta}),\,\nabla\delta u\rangle\,\mathrm{d}X \\
&\quad = -\int_\Omega \langle f,\,\delta u\rangle\,\mathrm{d}X\,, \qquad \text{(B.5a)} \\
&\int_\Omega -2\mu_\mathrm{e}\langle(\nabla u - \boldsymbol{\zeta}),\,\delta\boldsymbol{\zeta}\rangle + 2\mu_\mathrm{micro}\,\langle\boldsymbol{\zeta},\,\delta\boldsymbol{\zeta}\rangle \\
&\quad + \mu_\mathrm{macro}\,L_\mathrm{c}^2\,\langle\mathrm{curl}_\mathrm{2D}\,\boldsymbol{\zeta},\,\mathrm{curl}_\mathrm{2D}\,\delta\boldsymbol{\zeta}\rangle\,\mathrm{d}X \\
&\quad - \mu_\mathrm{macro}L_\mathrm{c}^2\oint_{\partial\Omega}\mathrm{curl}_\mathrm{2D}\,\boldsymbol{\zeta}\,\langle\delta\boldsymbol{\zeta},\,\boldsymbol{\tau}\rangle\,\mathrm{d}s \\
&\quad = \int_\Omega \langle\boldsymbol{\omega},\,\delta\boldsymbol{\zeta}\rangle\,\mathrm{d}X\,. \qquad \text{(B.5b)}
\end{aligned}$$

The latter integrations generate terms for transmissions on the boundary $\partial\Omega$. As the Dirichlet data is directly incorporated into the space and the natural Neumann boundary conditions Eqs. (2.6e) and (2.6f) hold, we observe

$$\begin{aligned}
&\int_{\Gamma_N^u} 2\mu_\mathrm{e}\,\delta u\langle(\nabla u - \boldsymbol{\zeta}),\,\boldsymbol{\nu}\rangle\,\mathrm{d}s = 0\,, \\
&\int_{\Gamma_N^\zeta}\mathrm{curl}_\mathrm{2D}\,\boldsymbol{\zeta}\,\langle\delta\boldsymbol{\zeta},\,\boldsymbol{\tau}\rangle\,\mathrm{d}s = 0\,, \qquad \text{(B.6)}
\end{aligned}$$

allowing us to find the original weak formulation with the corresponding force and moment

$$\begin{aligned}
&\int_\Omega 2\mu_\mathrm{e}\langle(\nabla u - \boldsymbol{\zeta}),\,\nabla\delta u\rangle\,\mathrm{d}X = \int_\Omega \langle f,\,\delta u\rangle\,\mathrm{d}X\,, \\
&\int_\Omega -2\mu_\mathrm{e}\langle(\nabla u - \boldsymbol{\zeta}),\,\delta\boldsymbol{\zeta}\rangle + 2\mu_\mathrm{micro}\,\langle\boldsymbol{\zeta},\,\delta\boldsymbol{\zeta}\rangle \\
&\quad + \mu_\mathrm{macro}\,L_\mathrm{c}^2\,\langle\mathrm{curl}_\mathrm{2D}\,\boldsymbol{\zeta},\,\mathrm{curl}_\mathrm{2D}\,\delta\boldsymbol{\zeta}\rangle\,\mathrm{d}X = \int_\Omega \langle\boldsymbol{\omega},\,\delta\boldsymbol{\zeta}\rangle\,\mathrm{d}X\,. \qquad \text{(B.7)}
\end{aligned}$$

References

1. Abdulle A (2006) Analysis of a heterogeneous multiscale FEM for problems in elasticity. Math Models Methods Appl Sci 16(04):615–635
2. Aivaliotis A, Daouadji A, Barbagallo G, Tallarico D, Neff P, Madeo A (2018) Low-and high-frequency stoneley waves, reflection and transmission at a Cauchy/relaxed micromorphic interface. arXiv:1810.12578
3. Aivaliotis A, Daouadji A, Barbagallo G, Tallarico D, Neff P, Madeo A (2019) Microstructure-related stoneley waves and their effect on the scattering properties of a 2D Cauchy/relaxed-micromorphic interface. Wave Motion 90:99–120
4. Anjam I, Valdman J (2015) Fast MATLAB assembly of FEM matrices in 2d and 3d: edge elements. Appl Math Comput 267:252–263
5. Askes H, Aifantis E (2011) Gradient elasticity in statics and dynamics: an overview of formulations, length scale identification procedures, finite element implementations and new results. Int J Solids Struct 48:1962–1990
6. Braess D (2013) Finite Elemente - Theorie, schnelle Löser und Anwendungen in der Elastizitätstheorie, 5th edn. Springer-Verlag, Berlin
7. d'Agostino MV, Barbagallo G, Ghiba ID, Eidel B, Neff P, Madeo A (2020) Effective description of anisotropic wave dispersion in mechanical band-gap metamaterials via the relaxed micromorphic model. J Elast 139(2):299–329
8. Demkowicz L (2006) Computing with hp-adaptive finite elements. One- and two-dimensional elliptic and maxwell problems, vol 1. Chapman and Hall/CRC, London
9. Demkowicz L, Kurtz J, Pardo D, Paszynski M, Rachowicz W, Zdunek A (2007) Computing with hp-adaptive finite elements. Frontiers: three-dimensional elliptic and maxwell problems with applications, vol 2. Chapman and Hall/CRC, London
10. Efendiev Y, Hou T (2009) Multiscale finite element methods. Springer-Verlag, New York
11. Eidel B, Fischer A (2018) The heterogeneous multiscale finite element method for the homogenization of linear elastic solids and a comparison with the FE^2 method. Comput Methods App Mech Eng 329:332–368
12. Eringen A (1999) Microcontinuum field theories. I. Foundations and solids. Springer-Verlag, New York
13. Forest S, Sievert R (2006) Nonlinear microstrain theories. Int J Solids Struct 43(24):7224–7245
14. Ghiba ID, Neff P, Owczarek S (2021) Existence results for non-homogeneous boundary conditions in the relaxed micromorphic model. Math Methods Appl Sci 44(2):2040–2049
15. Hütter G (2016) Application of a microstrain continuum to size effects in bending and torsion of foams. Int J Eng Sci 101:81–91
16. Jeong J, Neff P (2010) Existence, uniqueness and stability in linear Cosserat elasticity for weakest curvature conditions. Math Mech Solids 15(1):78–95
17. Kirchner N, Steinmann P (2006) Mechanics of extended continua: modeling and simulation of elastic microstretch materials. Comput Mech 40(4):651
18. Lehrenfeld C, Schöberl J (2016) High order exactly divergence-free hybrid discontinuous Galerkin methods for unsteady incompressible flows. Comput Methods Appl Mech Eng 307:339–361
19. Madeo A, Barbagallo G, Collet M, dAgostino MV, Miniaci M, Neff P (2018) Relaxed micromorphic modeling of the interface between a homogeneous solid and a band-gap metamaterial: new perspectives towards metastructural design. Math Mech Solids 23(12):1485–1506
20. Madeo A, Neff P, Ghiba ID, Rosi G (2016) Reflection and transmission of elastic waves in non-local band-gap metamaterials: a comprehensive study via the relaxed micromorphic model. J Mech Phys Solids 95:441–479
21. Meunier G (2010) The finite element method for electromagnetic modeling. Wiley-ISTE, United States
22. Mindlin R (1964) Micro-structure in linear elasticity. Arch Ration Mech Anal 16:51–78
23. Mindlin RD, Eshel NN (1968) On first strain-gradient theories in linear elasticity. Int J Solids Struct 4(1):109–124
24. Monk P (2003) Finite element methods for Maxwell's Equations. Numerical mathematics and scientific computation. Oxford University Press, New York
25. Münch I, Neff P, Madeo A, Ghiba ID (2017) The modified indeterminate couple stress model: why Yang et al.'s arguments motivating a symmetric couple stress tensor contain a gap and why the couple stress tensor may be chosen symmetric nevertheless. Zeitschrift für Angewandte Mathematik und Mechanik 97(12):1524–1554
26. Münch I, Neff P, Wagner W (2011) Transversely isotropic material: nonlinear Cosserat versus classical approach. Contin Mech Thermodyn 23(1):27–34
27. Nedelec JC (1980) Mixed finite elements in $\mathbb{R}^3$. Numerische Mathematik 35(3):315–341
28. Nédélec JC (1986) A new family of mixed finite elements in $\mathbb{R}^3$. Numerische Mathematik 50(1):57–81
29. Neff P, Eidel B, d'Agostino MV, Madeo A (2020) Identification of scale-independent material parameters in the relaxed micromorphic model through model-adapted first order homogenization. J Elast 139(2):269–298
30. Neff P, Forest S (2007) A geometrically exact micromorphic model for elastic metallic foams accounting for affine microstructure. Modelling, existence of minimizers, identification of moduli and computational results. J Elast 87(2):239–276
31. Neff P, Ghiba ID, Madeo A, Placidi L, Rosi G (2014) A unifying perspective: the relaxed linear micromorphic continuum. Contin Mech Thermodyn 26(5):639–681
32. Neff P, Jeong J, Ramézani H (2009) Subgrid interaction and micro-randomness - novel invariance requirements in infinitesimal gradient elasticity. Int J Solids Struct 46(25):4261–4276
33. Neff P, Madeo A, Barbagallo G, D'Agostino MV, Abreu R, Ghiba ID (2017) Real wave propagation in the isotropic-relaxed micromorphic model. Proceed R Soc A Math Phys Eng Sci 473:2197
34. Owczarek S, Ghiba ID, Neff P (2020) A note on local higher regularity in the dynamic linear relaxed micromorphic model. submitted. arXiv:2006.05448
35. Rizzi G, Hütter G, Madeo A, Neff P (2021) Analytical solutions of the simple shear problem for micromorphic models and other generalized continua. Arch Appl Mech. https://doi.org/10.1007/s00419-021-01881-w
36. Rizzi G, Htter G, Khan H, Madeo A, Neff P. Analytical solution of the cylindrical torsion problem for the relaxed micromorphic continuum and other generalized continua (including full derivations) (in preparation)
37. Rizzi G, Htter G, Madeo A, Neff P (2021) Analytical solutions of the cylindrical bending problem for the relaxed micromorphic continuum and other generalized continua (including full derivations). to appear in continuum mechanics and thermodynamics. arXiv:2012.10391
38. Romeo M (2020) A microstretch continuum approach to model dielectric elastomers. Zeitschrift für angewandte Mathematik und Physik 71(2):44
39. Schöberl J (1997) NETGEN an advancing front 2D/3D-mesh generator based on abstract rules. Comput Vis Sci 1(1):41–52
40. Schöberl J (2014) C++ 11 implementation of finite elements in NGSolve. Institute for analysis and scientific computing, Vienna University of Technology. URL https://www.asc.tuwien.ac.at/~schoeberl/wiki/publications/ngs-cpp11.pdf

41. Schöberl J, Zaglmayr S (2005) High order Nédélec elements with local complete sequence properties. COMPEL - Int J Comput Math Electr Electron Eng 24(2):374–384
42. Steigmann DJ (2012) Theory of elastic solids reinforced with fibers resistant to extension, flexure and twist. Int J Non-Linear Mech 47(7):734–742
43. Voss J, Baaser H, Martin RJ, Neff P (2020) More on anti-plane shear. J Optim Theory Appl 184(1):226–249
44. Zaglmayr S (2006) High order finite element methods for electromagnetic field computation. Ph.D. thesis, Johannes Kepler Universität Linz. URL https://www.numerik.math.tugraz.at/~zaglmayr/pub/szthesis.pdf